A large topographic feature on the surface of the trans-Neptunian object (307261) 2002 MS$_4$ measured from stellar occultations[*]

F. L. Rommel[1,2,3], F. Braga-Ribas[3,1,2], J. L. Ortiz[4], B. Sicardy[5], P. Santos-Sanz[4], J. Desmars[6,7],
J. I. B. Camargo[1,2], R. Vieira-Martins[1,2], M. Assafin[8,2], B. E. Morgado[8,2,1], R. C. Boufleur[1,2],
G. Benedetti-Rossi[9,5,2], A. R. Gomes-Júnior[10,9,2], E. Fernández-Valenzuela[11], B. J. Holler[12],
D. Souami[5,13,14,**], R. Duffard[4], G. Margoti[3,2], M. Vara-Lubiano[4], J. Lecacheux[5], J. L. Plouvier[15], N. Morales[4],
A. Maury[16], J. Fabrega[17], P. Ceravolo[18], E. Jehin[19], D. Albanese[20], H. Mariey[21], S. Cikota[22,23], D. Ruždjak[24],
A. Cikota[25], R. Szakáts[26,27], D. Baba Aissa[28], Z. Gringahcene[28], V. Kashuba[29], N. Koshkin[29], V. Zhukov[30],
S. Fişek[31,32], O. Çakır[33,34], S. Özer[35,36], C. Schnabel[37,38], M. Schnabel[38], F. Signoret[39], L. Morrone[40,41],
T. Santana-Ros[42,43], C. L. Pereira[1,2,3], M. Emilio[44,1,3], A. Y. Burdanov[45], J. de Wit[45], K. Barkaoui[46,45,47],
M. Gillon[46], G. Leto[48], A. Frasca[48], G. Catanzaro[48], R. Zanmar Sanchez[48], U. Tagliaferri[49], M. Di Sora[49],
G. Isopi[49], Y. Krugly[50,51], I. Slyusarev[50], V. Chiorny[50], H. Mikuž[52,53], P. Bacci[54], M. Maestripieri[54],
M. D. Grazia[54], I. de la Cueva[55], M. Yuste-Moreno[55], F. Ciabattari[56], O. M. Kozhukhov[57], M. Serra-Ricart[47,58],
M. R. Alarcon[47,58], J. Licandro[47,58], G. Masi[59], R. Bacci[60], J. M. Bosch[61], R. Behem[62], J.-P. Prost[62],
S. Renner[7,63], M. Conjat[21], M. Bachini[64], G. Succi[64], L. Stoian[65], A. Juravle[65], D. Carosati[66], B. Gowe[67], J. Carrillo[68],
A. P. Zheleznyak[50], N. Montigiani[69], C. R. Foster[70], M. Mannucci[69], N. Ruocco[71], F. Cuevas[72],
P. Di Marcantonio[73], I. Coretti[73], G. Iafrate[73], V. Baldini[73], M. Collins[74], A. Pál[26], B. Csák[26],
E. Fernández-Garcia[4], A. J. Castro-Tirado[4], L. Hudin[75], J. M. Madiedo[4], R. M. Anghel[76], J. F. Calvo-Fernández[77],
A. Valvasori[78,79], E. Guido[80], R. M. Gherase[81], S. Kamoun[82,83], R. Fafet[62], M. Sánchez-González[84,85],
L. Curelaru[86], C. D. Vîntdevară[87], C. A. Danescu[88], J.-F. Gout[89], C. J. Schmitz[90,***], A. Sota[4], I. Belskaya[5,50],
M. Rodríguez-Marco[91], Y. Kilic[92,93], E. Frappa[94], A. Klotz[95], M. Lavayssière[96], J. Marques Oliveira[5],
M. Popescu[88], L. A. Mammana[97,98], E. Fernández-Lajús[98,99], M. Schmidt[100], U. Hopp[100], R. Komžík[101],
T. Pribulla[101], D. Tomko[101], M. Husárik[101], O. Erece[93,92], S. Eryilmaz[93], L. Buzzi[102], B. Gährken[103,***],
D. Nardiello[104,105], K. Hornoch[106], E. Sonbas[107,108], H. Er[109], V. Burwitz[110], P. Waldemar Sybilski[111],
W. Bykowski[111], T. G. Müller[110], W. Ogloza[112], R. Gonçalves[113], J. F. Ferreira[114], M. Ferreira[115], M. Bento[115],
S. Meister[116,117], M. N. Bagiran[118], M. Tekeş[119,120], A. Marciniak[51], Z. Moravec[121], P. Delinčák[122,***],
G. Gianni[123], G. B. Casalnuovo[124], M. Boutet[125], J. Sanchez[126], B. Klemt[37,127], N. Wuensche[37],
W. Burzynski[128,129,37], M. Borkowski[130,***], M. Serrau[131], G. Dangl[37], O. Klös[37], C. Weber[37], M. Urbaník[132],
L. Rousselot[131], J. Kubánek[37,133,134], P. André[135], C. Colazo[136,137,138], J. Spagnotto[139], A. A. Sickafoose[140],
R. Hueso[141], A. Sánchez-Lavega[141], R. S. Fisher[142], A. W. Rengstorf[143], C. Perelló[38,37], M. Dascalu[144],
M. Altan[145], K. Gazeas[146], T. de Santana[5,9,147], R. Sfair[9,147], O. C. Winter[9], S. Kalkan[148], O. Canales-Moreno[38],
J. M. Trigo-Rodríguez[149], V. Tsamis[150], K. Tigani[150], N. Sioulas[151], G. Lekkas[152], D. N. Bertesteanu[81],
V. Dumitrescu[153,***], A. J. Wilberger[154], J. W. Barnes[155], S. K. Fieber-Beyer[156], R. L. Swaney[157],
C. Fuentes[158,159,160], R. A. Mendez[158], B. D. Dumitru[161], R. L. Flynn[162], and D. A. Wake[163]

(Affiliations can be found after the references)

ABSTRACT

Context. The physical characterization of trans-Neptunian objects is essential for improving our understanding of the formation and evolution of our Solar System. Stellar occultation is a ground-based technique that can be successfully used to determine some of the TNOs' fundamental physical properties with high precision, such as size and shape.
Aims. This work is aimed at constraining the size, shape, and geometric albedo of the dwarf planet candidate (307261) 2002 MS$_4$ through the analysis of nine stellar occultation events. Using multichord detection, we also study the object's topography by analyzing the obtained limb and residuals between the observed chords and the best-fit ellipse.

[*] Tables B.1–B.5 are available at the CDS via anonymous ftp to cdsarc.cds.unistra.fr (130.79.128.5) or via https://cdsarc.cds.unistra.fr/viz-bin/cat/J/A+A/678/A167
[**] Fulbright Visiting Scholar (2022–2023) at University of California, Berkeley.
[***] Private observer.

Methods. We predicted and organized the observational campaigns of nine stellar occultations by 2002 MS$_4$ between 2019 and 2022, resulting in two single-chord events, four double-chord detections, and three events with between 3 and 61 positive chords. We derived the occultation light curves using differential aperture photometry, from which the star ingress and egress instants were calculated. Using 13 selected chords from the 8 August 2020 event, we determined the global elliptical limb of 2002 MS$_4$. The best-fit ellipse, combined with the object's rotational information from the literature, sets constraints on the object's size, shape, and albedo. Additionally, we developed a new method to characterize the topography features on the object's limb.

Results. The global limb has a semi-major axis of $a' = 412 \pm 10$ km, a semi-minor axis of $b' = 385 \pm 17$ km, and the position angle of the minor axis is $121° \pm 16°$. From this instantaneous limb, we obtained 2002 MS$_4$'s geometric albedo of $p_V = 0.1 \pm 0.025$, using $H_V = 3.63 \pm 0.05$ mag and a projected area-equivalent diameter of 796 ± 24 km. Significant deviations from the fitted ellipse in the northernmost limb were detected from multiple sites, highlighting three distinct topographic features: one 11 km depth depression, followed by a 25^{+4}_{-5} km height elevation next to a crater-like depression, with an extension of 322 ± 39 km and 45.1 ± 1.5 km deep.

Conclusions. Our results indicate the presence of an object that is $\approx$138 km smaller in diameter than that derived from thermal data, possibly indicating the presence of a thus-far unknown satellite. However, within the error bars, the geometric albedo in the V-band is in agreement with the results published in the literature, even with the radiometric-derived albedo. This stellar occultation has allowed for the first multichord measurement of a large topography in a TNO.

Keywords: Kuiper belt objects: individual: 2002 MS4 – methods: observational

1. Introduction

Trans-Neptunian objects (TNOs) are small Solar System bodies that orbit the Sun with a semi-major axis larger than that of Neptune (Jewitt et al. 2008). Due to the low spatial density of material in this orbital region and the significant distance from the Sun, their global physical-chemical composition has been largely unaffected since their formation. Therefore, they are considered to be remnants of the primordial disk and a valuable source of information about the primitive solar nebula and the evolution of our planetary system (Gladman et al. 2008; Morbidelli et al. 2008; Nesvorný & Morbidelli 2012). In addition, knowledge of the size-frequency distribution of TNOs allows for constraints to be placed on Solar System formation models (Petit et al. 2008). Mainly due to the faintness and small angular sizes seen from Earth, our knowledge of the fundamental physical properties of the TNO population is still scarce and fragmented (Stansberry et al. 2008; Lellouch et al. 2013; Lacerda et al. 2014). Since the discovery of (15760) Albion in 1992 (Jewitt & Luu, 1993), thousands of objects have been observed in this orbital region. However, the size and albedo of only 178 Centaurs (objects with unstable orbits between Jupiter and Neptune) and TNOs have been determined using thermal observations (Müller et al. 2020). On the other hand, spacecraft visits can fully characterize these objects, as in the case of the visit of the New Horizons mission (Weaver and Stern 2008) to the Pluto system (Stern et al. 2015, 2020; Spencer et al. 2020 b) and (486958) Arrokoth (Stern et al. 2019; Benecchi et al. 2019; Buie et al. 2020 a; Spencer et al. 2020a), which allowed for detailed studies. However, the aforementioned approaches require significant investment and cannot be used to study a larger number of objects.

Stellar occultation is an efficient ground-based method to study dozens of these distant bodies. It consists of observing a background star while a small body passes in front of it and blocks the stellar flux for several seconds. An updated list of Lucky Star stellar occultation detections (that we are aware of) can be found in the SOSB Database[1] (Braga-Ribas et al. 2019). These observations provide an instantaneous limb of the object that can be combined with information derived from other observational methods to better characterize the small body (Ortiz et al. 2020b).

In this work, we predicted, observed, and analyzed nine stellar occultations by the large TNO (307261) 2002 MS$_4$ (hereafter denoted as MS4 for brevity). It was discovered by the Near-Earth Asteroid Tracking (NEAT)[2] program on June 18, 2002, and is classified as a hot classical TNO due to its high orbital inclination (Gladman et al. 2008; Van Laerhoven et al. 2019). Furthermore, MS4 is a candidate to be a dwarf planet due to its thermally derived equivalent diameter (Vilenius et al. 2012). Physical and orbital parameters taken from previously published works are listed in Table 1.

2. Predictions and observations

We performed classical astrometric runs to refine MS4's ephemeris at the Pico dos Dias (Brazil), La Silla (Chile), Calar Alto (Spain), and Pic du Midi (France) observatories between 2009 and 2019. The updated ephemeris and the *Gaia* Data Release 1 catalog (Gaia Collaboration 2016a,b, 2018) significantly improved the prediction of the July 9, 2019 occultation, resulting in our first occultation by MS4. Furthermore, the astrometry derived from this occultation data improved the subsequent predictions.

In 2019, we observed four stellar occultations by MS4 from Argentina, Brazil, Canada, and Chile (see Tables B.4 and B.5). On July 26, we obtained a multichord detection from three well-separated sites and about 8 h later, a single-chord occultation of a different star from Canada. On July 9 and August 19, we detected two positive chords and a set of negatives. The astrometric results from 2019 data were used to calculate new ephemeris and predict the subsequent events using the Numerical Integration of the Motion of an Asteroid (NIMA) tool described on Desmars et al. (2015)[3].

The first observation in 2020 was a double chord from South Africa on July 26, which confirmed the accuracy of MS4's ephemeris at an eight-milliarcsec (mas) level. Therefore, we organized an extensive campaign and successfully observed, from 61 sites, an occultation of a bright star ($V = 14.62$ mag) on August 8, 2020. As described in this work, we derived valuable physical information from this multichord event observed in North Africa, Europe, and Western Asia. After the 8 August 2020 campaign, three other events were observed on 24 February

---

[1] Stellar Occultation by Small Bodies database is available on `http://occultations.ct.utfpr.edu.br/results`

[2] More information available at `https://sbn.psi.edu/pds/resource/neat.html`

[3] MS4's ephemeris (NIMA v9) is publicly available on `https://lesia.obspm.fr/lucky-star/obj.php?p=692`

Table 1. Orbital and physical properties of MS4 from the literature.

Orbital properties [a]		Physical properties	
a	41.8 au	D [b]	934 ± 47 km
q	35.75 au	H_V	4.0 ± 0.6 [b]/3.63 [c]
i	17.7°	p_V [b]	$0.051^{+0.036}_{-0.022}$
e	0.14	Ap_{mag} [d]	20.39 mag

Notes. [a]Orbital elements from JPL Small-Boby Database Browser web page (`https://ssd.jpl.nasa.gov/tools/sbdb_lookup.html#/?sstr=2002MS4`). [b]Physical properties obtained by Vilenius et al. (2012): area-equivalent diameter (D) and geometric albedo at V-band (p_V); H_V: average absolute magnitude at V-band; Stansberry et al. (2008) obtained D = 726.05 ± 123.05 km and $p_V = 0.084^{+0.038}_{-0.023}$ for a value of H_V = 4.0 using *Spitzer* data only. [c]Information from Tegler et al. (2016). [d]Ap_{mag}: object's average apparent visual magnitude on August 8, 2020, from JPL website `https://ssd.jpl.nasa.gov/horizons/app.html#/`.

2021, 14 October 2021, and 10 June 2022. Single, double, and triple detections, respectively (Tables B.4 and B.5). Those data and equipment information collection processes were carried out through the Occultation Portal[4] (Kilic et al. 2022). Table 2 shows the relevant information about all the occulted stars from the *Gaia* Data Release 3 catalog (GDR3, Gaia Collaboration 2023).

The default procedure for all events was to update the prediction and send alerts to potential observers within or close to the predicted shadow path. However, an exception was made for the 8 August 2020 occultation due to favorable circumstances. A campaign web page with helpful information for the observers was built[5]. Also, alerts were sent to all individuals with access to portable or professional telescopes and near or inside the predicted shadow path, resulting in such a large number of positive detections.

The data came from a wide range of telescopes, from small portable ones (apertures between 13 cm and 30 cm) to large facilities such as the 4.1 m telescope at the Southern Astrophysical Research (SOAR, Chile), the 2 m Liverpool telescope at Roque de Los Muchachos (Spain), the 1.6 m telescope at Pico dos Dias (Brazil), and the 1.5 m telescope at Sierra Nevada (Spain) observatories. Most observers did not use filters to maximize photon fluxes on the CCD and so, they were able to a better signal-to-noise ratio (S/N). Even though some observers used the Global Positioning System (GPS) to acquire the time, the most common time source was the computer clock synchronization with a Network Time Protocol (NTP). A compilation of all the participating observers and instruments is presented in Appendix B. All the predictions and observational efforts were developed in the framework of the European Research Council (ERC) Lucky Star project[6].

3. Data reduction, analysis, and results

The great diversity of telescopes and detectors was reflected in five data formats[7]: *avi*, *adv* (Pavlov et al. 2020), *ser*, *cpa*, and

FITS. Most *avi*, *adv*, and *ser* video files were converted to FITS images using TANGRA[8] software. However, from some videos, the images were extracted using a proprietary PYTHON 3 script based on ASTROPY v4.0.1 (Astropy Collaboration 2013). When calibration images were available, the raw images were corrected from any bias, dark, and flat-field using standard procedures with the Image Reduction and Analysis Facility (IRAF, Butcher & Stevens, 1981).

We applied aperture photometry on the target and some comparison stars on all the FITS files using the Package for the Reduction of Astronomical Images Automatically (PRAIA, Assafin et al. 2011, 2023). The chosen photometric apertures considered the maximization of the S/N. The light curve obtained for the target star, which includes less than 1% of flux contributions from MS4, is then divided by the averaged light curves of the comparison stars to account for sky transparency variations in the data. Also, the flux outside the occultation is normalized to unity by fitting a polynomial function. Finally, the ingress and egress times were derived using the standard chi-square method (χ^2 test) between the observed and a synthetic light curve implemented in the Stellar Occultation Reduction and Analysis package, v0.2.1 (SORA, Gomes-Júnior et al. 2022). The synthetic light curve considers a sharp-edge model convolved with Fresnel diffraction, finite exposure time, CCD bandwidth, and stellar diameter at MS4's distance (details about this procedure are available in Gomes-Júnior et al. 2022 and references therein). The stellar diameters projected at MS4 distance were calculated according to Kervella et al. (2004)'s formalism and are listed in Table 2. Organized by the occultation date, Table 3 contains the ingress and egress times (UTC) with 1σ uncertainties for each station with a positive detection. Appendix C presents the normalized and the synthetic light curves used to obtain the occultation timings.

If not differentiated, large TNOs such as MS4 may reach one of the hydrostatic equilibrium shapes: the Jacobi three-axial ellipsoid or the Maclaurin oblate spheroid (Chandrasekhar 1987; Tancredi and Favre 2008). The apparent global limb of the body is then an ellipse projected in the sky plane, defined by $M = 5$ free parameters: center offset relative to the ephemeris (f and g), the semi-major axis (a'), the semi-minor axis (b'), or equivalently, the oblateness [$\epsilon' = (a' - b')/a'$], and the position angle (PA) of b'. The PA counts positively, starting from the celestial north and increasing to the east. We converted the ingress and egress times into a stellar position for each stellar occultation event, with f and g increasing toward celestial east and north, respectively. At this point, we can fit a limb model to these points, which provides, among others, the position of MS4's center in the sky plane and, thus, an ephemeris offset.

Among the nine stellar occultation events, only three allow for an elliptical fit to the chords, namely: 9 July 2019, 8 August 2020, and 10 June 2022. We started our fitting procedure with the 61 chords acquired on 8 August 2020 (Sect. 3.1), and we then used the residuals of the elliptic limb fit to search for topographic features on MS4 (Sect. 3.2). Finally, we compared

---

[4] More information on `https://occultation.tug.tubitak.gov.tr/about/`

[5] The campaign web page is available in `https://lesia.obspm.fr/lucky-star/campaigns/2020-08-08_2002MS4.html`

[6] `https://lesia.obspm.fr/lucky-star/`

[7] *avi* = Audio Video Interleave. Information for the *adv* (Astronomical Digital Video) can be found in

`https://www.iota-es.de/JOA/JOA2020_3.pdf`. The documentation for the simple image sequence format known as *ser* can be found in `http://www.grischa-hahn.homepage.t-online.de/astro/ser/`. *cpa* is a compressed image file associated with PRISM (`http://www.prism-astro.com/fr/index.html`). The most recent Flexible Image Transport System-FITS documentation can be found in `https://fits.gsfc.nasa.gov/fits_standard.html`

[8] `http://www.hristopavlov.net/Tangra3/`

Table 2. Target stars designation and geocentric coordinates at closest approach instant (UT) sorted by occultation date (day-month-year).

Date	Gaia DR3 designation	Propagated right ascension (hh mm ss.sssss)	Error (mas)	Propagated declination (° ' ")	Error (mas)	$V^{(a)}$ (mag)	$K^{(a)}$ (mag)	$S_{\mathrm{Diam}}^{(b)}$ (km)	$\Delta_{MS4}^{(c)}$ (au)
09-07-2019	4253196402592965504	18 45 19.24565	0.15	−06 24 13.0031	0.12	15.00	14.15	0.19	45.62
26-07-2019	4253186506987951104	18 44 07.57274	0.54	−06 26 40.1240	0.46	17.78	16.27	0.08	45.67
	4253186477047835648	18 44 06.31756	0.13	−06 26 43.8948	0.11	15.45	11.66	0.98	45.68
19-08-2019	4253181804071259648	18 42 43.51905	0.24	−06 32 34.0868	0.19	16.51	16.59	0.05	45.88
26-07-2020	4253244201379441792	18 48 18.07372	0.12	−06 13 31.6134	0.12	14.76	12.61	0.47	45.60
08-08-2020	4253248324549054464	18 47 29.96384	0.12	−06 16 31.4727	0.10	14.62	11.13	1.19	45.70
24-02-2021	4253709191700784896	18 56 35.98731	0.25	−06 30 23.1569	0.23	16.51	12.96	0.53	47.05
14-10-2021	4252495635735083264	18 50 30.76176	0.31	−06 24 13.3375	0.27	15.83	13.44	0.34	46.52
10-06-2022	4253907305577009664	19 00 15.44628	0.23	−05 42 42.9960	0.21	15.1	13.00	0.39	45.48

Notes. It is essential to mention that none of the stars have a duplicity flag in the Gaia DR3 catalog. $^{(a)}$The magnitudes retrieved from NOMAD catalog and used in SORA to calculate the $^{(b)}$stellar diameter (S_{Diam}) at the $^{(c)}$MS4's geocentric distance (Δ_{MS4}).

the resulting global ellipse with the chords observed in the other events (Sect. 3.3).

3.1. 8 August 2020

Three circumstances triggered an extensive observational campaign for this occultation: i) the bright target star ($G = 14.6$ mag from GDR3 catalog), ii) a milliarcsecond-level accuracy of MS4's ephemeris stemming from previously detected occultations, and iii) a shadow path crossing densely populated regions. Accordingly, the observational campaign motivated the participation of 116 telescopes from Europe, North Africa, and Western Asia. As a result, we received 61 positive and 40 negative data sets. The other 15 locations had bad weather conditions, and observers could not acquire data. The number of effective chords is smaller than the 61 positives due to overlapping observations from nearby observatories along the object's limb.

We then submitted all the images to the procedure described at the beginning of this section. As absolute time acquisition is essential to achieve good results, we checked each data set and applied offsets when: i) the observer reported time issues during the acquisition, ii) the camera acquisition software is known to have a systematic offset, and iii) overlapped chords that do not match the ingress and egress instants. In this last case, the time shifts applied to the original positive data were based on comparison with close-by chords. All the time shifts are presented in Table B.1, and the corrected instants are in Table 3. Figure 1 shows all the positives (blue lines) and their uncertainties in ingress and egress times (red segments).

A simple elliptical model cannot effectively reproduce the observed profile projected at the sky plane. However, a global profile can be obtained by selecting 13 positive chords among the 61 positives. The first selection criterion was the time source, namely, data acquired with GPS were preferred. Among the 17 GPS data sets, we discarded the following: 1) Varages because it presented a gradual emersion in the light curve (see Sect. 3.2); 2) Nice due to reported time issues during the acquisition; 3) Khmelnytskyi and Sevilla because it probed the latitude where a large topography is suspected (see Sect. 3.2); 4) Guarcino because the GPS was connected to the computer and it presented a large offset with respect to all close-by chords; 5) Artemis because its length does not match the length of Catania's chord

(at 1σ level), which probed exactly the same object's profile but is a bit larger. 6) Finally, Caussols, Ariana, and Kuban have larger uncertainties than other chords that probed the same region. In addition to the eight GPS data sets, we selected another five positive chords acquired from Méo station, Mátraszentistván, Hvar, Agerola, and La Palma. The main criteria for selecting the mentioned NTP chords were: data acquired with professional telescopes, low dispersion in the light curves, and the smallest uncertainties of the probed limb.

Figure 2 presents the 13 selected positive chords (blue) over-plotted to the other positives (gray segments). Solid lines represent GPS chords, while dashed lines show NTP data. The selected data are ordered from north to south, as follows: Méo station (FRA), Valbonne (FRA), Mátraszentistván (HUN), Catalonia (ESP), Massa (ITA), Rome (ITA), Hvar (HRV), Sassari (ITA), Odesa (UKR), Agerola (ITA), Algiers (DZA), La Palma (ESP), and Çanakkale (TUR). They provide $N = 26$ independent points at the sky plane to fit the five ellipse parameters. The global elliptical limb is determined by minimizing the classical χ^2 function. The quality of the result is given by the χ^2 per degree of freedom $\chi^2_{\mathrm{pdf}} = \chi^2/(N - M) \approx 1$ for satisfactory fits, where N is the number of points and M is the number of fitted parameters (Gomes-Júnior et al. 2022). A set of empirical tests[9] assuming topography values between 0 and 10 km were performed and revealed a good fit ($\chi^2_{\mathrm{pdf}} = 0.92$) when features of 7 km were considered. This result agrees with the theoretical approach proposed by Johnson and McGetchin (1973), which gives a lower limit of 6–7 km for topography on MS4 (see Sect. 3.4).

Among the elliptical solutions inside the 3σ region, we excluded those that crossed or approached the negative grazing chords within the tolerance level of 7 km (radial direction). Therefore, although the solutions cross the negative chord as seen from Montsec (Fig. 2), they are inside the 7 km assumed range. The area equivalent radius was calculated using the relation $R_{\mathrm{equiv}} = a' \sqrt{1 - \epsilon'}$. Finally, the limb solution in Table 4 represents the best-fitted elliptical limb at the sky plane with uncertainties at the 3σ level.

---

9 See Eq. (11) in Gomes-Júnior et al. (2022) for details about the function that considers topography in the limb fitting.

Table 3. Ingress and egress instants with 1σ error bars.

Sites	Ingress (hh:mm:ss.ss ± ss.ss)	Egress (hh:mm:ss.ss ± ss.ss)
09 July 2019		
OPSPA	04:23:28.65 ± 0.19	04:23:58.26 ± 0.38
ASH2	04:23:27.2 ± 1.1	04:23:56.73 ± 2.1
Pico dos Dias	04:22:02.182 ± 0.006	04:22:29.44 ± 0.67
26 July 2019 – South America		
OPSPA	02:47:15.6 ± 7.8	02:48:04.0 ± 3.7
ASH2	02:47:21.0 ± 3.8	02:47:54.8 ± 5.3
Paranal	02:47:34.33 ± 0.12	02:48:07.9 ± 1.2
Pico dos Dias	02:45:55.310 ± 0.099	02:46:17.581 ± 0.093
26 July 2019 – North America		
Osoyoos	10:15:16.65 ± 0.40	10:15:53.12 ± 0.33
19 August 2019		
Penticton	07:37:19.2 ± 2.6	07:37:55.2 ± 1.3
Osoyoos	07:37:17.55 ± 0.55	07:37:53.7 ± 2.0
26 July 2020		
Pretoria	23:15:28.46 ± 0.12	23:15:54.27 ± 0.15
Johannesburg	23:15:28.940 ± 0.092	23:15:55.89 ± 0.18
08 August 2020		
Varages	20:43:44.858 ± 0.058	20:43:53.359 ± 0.028
TAROT North	20:43:39.5 ± 2.0	20:43:51.5 ± 2.0
Méo station	20:43:39.488 ± 0.021	20:43:53.960 ± 0.027
Caussols	20:43:39.27 ± 0.13	20:43:54.18 ± 0.56
Lleida	20:44:01.4 ± 6.6	20:44:25.13 ± 0.12
Cannes	20:43:37.23 ± 0.21	20:43:55.64 ± 0.39
Nice	20:43:36.444 ± 0.029	20:43:52.834 ± 0.071
Valbonne	20:43:37.376 ± 0.055	20:43:54.07 ± 0.13
Črni Vrh	20:43:09.71 ± 0.94	20:43:26.58 ± 0.35
Mátraszentistván	20:42:46.866 ± 0.015	20:43:04.739 ± 0.045
Ljubljana	20:43:06.70 ± 0.20	20:43:25.20 ± 0.33
Budapest	20:42:49.59 ± 0.13	20:43:08.61 ± 0.20
Trieste	20:43:07.7 ± 3.3	20:43:27.41 ± 0.85
Catalonia	20:43:57.15 ± 0.21	20:44:17.84 ± 0.14
Bologna	20:43:17.40 ± 0.26	20:43:38.77 ± 0.67
Massa 02	20:43:20.52 ± 0.39	20:43:43.83 ± 0.32
Castelvecchio Pascoli	20:43:18.742 ± 0.088	20:43:44.1 ± 1.4
Borgo a Mozzano	20:43:19.224 ± 0.078	20:43:42.80 ± 0.12
San Marcello Pistoiese	20:43:16.200 ± 0.072	20:43:42.6 ± 1.2
Sta. Maria a Monte	20:43:17.68 ± 0.12	20:43:42.80 ± 0.11
Signa	20:43:15.61 ± 0.57	20:43:40.38 ± 0.67
Lastra a Signa	20:43:13.815 ± 0.084	20:43:41.9 ± 1.2
Khmelnytskyi	20:42:01.81 ± 0.82	20:42:49.7 ± 15.7
Sevilla	20:44:29.03 ± 0.13	20:44:59.40 ± 0.19
Huelva	20:44:32.74 ± 0.37	20:45:02.72 ± 0.28
Cluj-Napoca	20:42:25.0 ± 1.2	20:42:56.61 ± 0.30
Fuensanta de Martos	20:44:22.0 ± 3.0	20:44:55.0 ± 3.1
Fiastra	20:43:05.1 ± 1.8	20:43:37.89 ± 0.52
Dragsina	20:42:32.938 ± 0.087	20:43:05.82 ± 0.32
Ibiza	20:43:56.6 ± 1.8	20:44:28.55 ± 0.24
Alhendín	20:44:17.89 ± 0.57	20:44:54.83 ± 0.18
Granada (150 cm)	20:44:17.571 ± 0.008	20:44:52.08 ± 0.51
Granada (90 cm)	20:44:16.53 ± 0.51	20:44:51.755 ± 0.026
Estepona	20:44:24.37 ± 0.45	20:45:00.4 ± 1.9
Marbella	20:44:26.1 ± 4.3	20:44:59.64 ± 0.22
Rome	20:43:08.37 ± 0.37	20:43:43.79 ± 0.37
Hvar	20:42:51.69 ± 0.21	20:43:27.96 ± 0.35
Bacau	20:42:12.60 ± 0.30	20:42:50.49 ± 0.72
Sassari	20:43:19.35 ± 0.35	20:43:56.60 ± 0.50
Guarcino	20:43:03.86 ± 0.15	20:43:41.13 ± 0.15
Kharkiv (70 cm)	20:41:40.00 ± 0.13	20:42:17.16 ± 0.12
Kharkiv (36 cm)	20:41:39.6 ± 1.9	20:42:18.3 ± 1.2
Ceccano	20:43:02.39 ± 0.41	20:43:40.76 ± 0.37
Brasov	20:42:14.2 ± 2.7	20:42:51.5 ± 1.6
Bârlad	20:42:09.23 ± 0.55	20:42:47.00 ± 0.49
Valenii de Munte	20:42:15.14 ± 0.24	20:42:52.61 ± 0.50
Ploiesti	20:42:14.25 ± 2.1	20:42:53.2 ± 1.5

Table 3. continued.

Sites	Ingress (hh:mm:ss.ss ± ss.ss)	Egress (hh:mm:ss.ss ± ss.ss)
Odesa	20:42:00.00 ± 0.14	20:42:38.49 ± 0.11
Sorrento	20:43:00.66 ± 0.30	20:43:37.7 ± 1.1
Agerola	20:42:59.603 ± 0.050	20:43:37.842 ± 0.093
Algiers	20:43:50.844 ± 0.021	20:44:29.115 ± 0.075
La Palma	20:45:35.032 ± 0.014	20:46:08.313 ± 0.018
Tijarafe	20:45:35.68 ± 0.19	20:46:08.08 ± 0.11
Ariana	20:43:23.87 ± 0.29	20:43:56.80 ± 0.25
Artemis	20:45:31.938 ± 0.022	20:46:01.297 ± 0.024
TAR 1	20:45:32.360 ± 0.057	20:46:01.595 ± 0.063
Catania	20:43:04.59 ± 0.92	20:43:34.564 ± 0.085
Kuban	20:41:36.2 ± 1.2	20:42:00.63 ± 0.31
Çanakkale	20:42:23.39 ± 0.56	20:42:38.830 ± 0.072
24 February 2021		
OPSPA	08:41:37.00 ± 0.61	08:42:09.182 ± 0.082
ASH2	08:41:36.82 ± 0.98	08:42:08.43 ± 0.30
14 October 2021		
Osoyoos	03:23:30.14 ± 0.40	03:24:35.33 ± 0.67
Flagstaff	03:25:54.61 ± 0.44	03:26:39.33 ± 0.73
10 June 2022		
La Palma	05:30:08.475 ± 0.091	05:30:43.30 ± 0.13
Artemis	05:30:02.427 ± 0.066	05:30:37.51 ± 0.49
Tree Gate Farm	05:34:47.18 ± 0.33	05:35:22.12 ± 0.28

Notes. The table lines are sorted from northernmost to southernmost, regarding the object's latitude probed by the observatory and separated by event date.
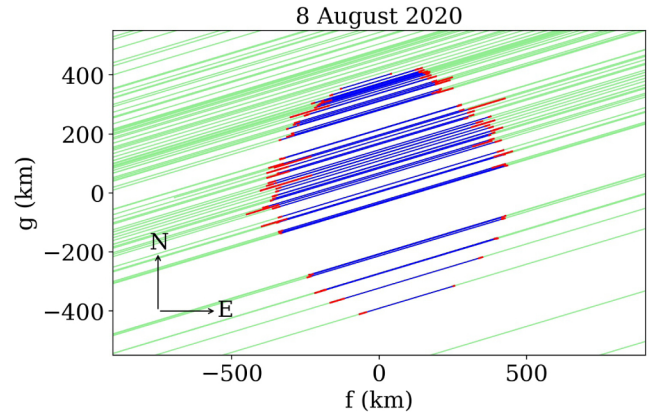

Fig. 1. Chords measured during the 8 August 2020 event show the detection of MS4's limb in blue with 1σ error bars (red segments). Six positive chords with large error bars were suppressed from this plot for better visualization: TAROT, Lleida, Khmelnytskyi, Fuensanta de Martos, Kharkiv T36, and Marbella. The green lines represent positions compatible with the total target's flux within the noise (i.e., no secondary occultation). The order of positive chords, from north to south, is the same as in Table 3.

Table 4. Parameters of the best-fitted ellipse (at 3σ level) derived from the 13 selected positive chords from the August 8 event.

MS4's global elliptical limb[a]					
f	43 ± 6 km	a'	412 ± 10 km	PA	121 ± 16°
g	7 ± 9 km	ϵ'	0.066 ± 0.034	R_{equiv}	398 ± 12 km

Notes. [a] These solutions admit topographic features up to 7 km and are limited to the north by the negative chord from the Montsec station (orange segments in Fig. 2).
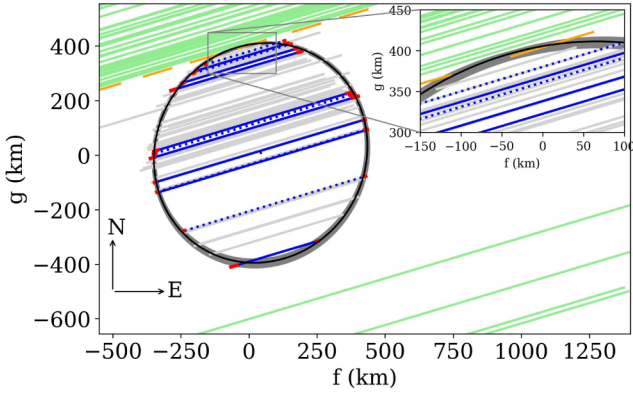
Fig. 2. Thirteen selected chords (blue), where GPS data are presented in solid lines and NTP by dashed lines. Gray segments show the other positive chords not used in limb-fitting. The black ellipse shows the best elliptical limb, and the gray region the solutions within 3σ. The orange segments represent each image acquired from the Montsec station and the light green segments show other negative chords.
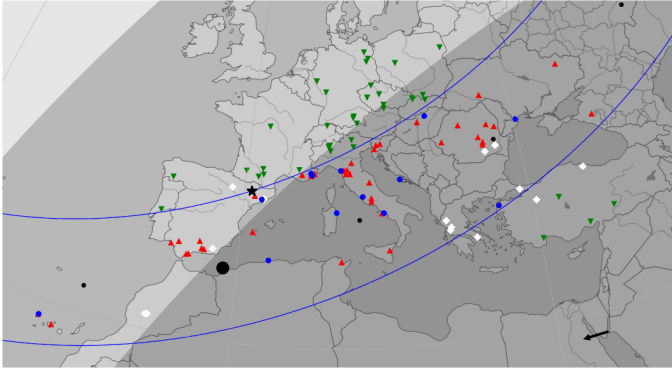

Fig. 3. Post-occultation map showing the location of each station that participated in the 8 August 2020 occultation campaign. Solid lines delimit the observed shadow path, and the black dots mark the shadow position every minute, with the largest at the moment of the geocenter's closest approach. The shadow follows the direction given by the black arrow. The blue dots indicate the 13 selected chords, while the other positives are in red triangles. A black star marks the close-by negative chord acquired from Montsec station. Green triangles and white diamonds represent stations with negative data and bad weather, respectively.

A general view of the August 2020 event is shown in Fig. 3. The blue lines represent the observed shadow path. It is worth mentioning that the 13 selected chords are in blue circles, and the other positives are in red triangles. We note that a black star marks the negative detection by Montsec station, while the green triangles mark the other negatives observations.

3.2. Topographic features

Determining the topographic limits for small bodies in the outer Solar System is challenging. The first attempts were theoretical; for instance, Johnson and McGetchin (1973) proposed a method to determine topography limits for planetary satellites using their global density and composition. On the other hand, from an observational point of view, just a few small bodies orbiting the Sun beyond Neptune had their topography limits set using stellar occultations (Dias-Oliveira et al. 2017; Leiva et al.
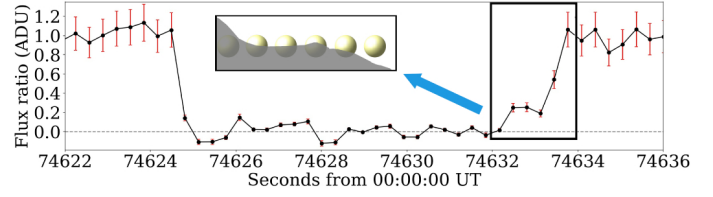
Fig. 4. Normalized stellar flux in each frame acquired in Varages station as a function of time in black dots, with photometric uncertainties in red. The insert selects the egress region and illustrates a possible explanation for such a signal (see text).

2017). Also, with the advance in interplanetary spacecraft technology, the surface of a few objects was studied using in situ images. For instance, using Voyager's images of Uranus's largest satellites Schenk and Moore (2020) found superficial features up to 11 km. Likewise, New Horizons' flyby over the Pluto system (Moore et al. 2016; Nimmo et al. 2017) and (486958) Arrokoth (Spencer et al. 2020a) revealed superficial structures on the same scale.

Applying the theoretical approach mentioned above for MS4 and assuming an icy body with a density between $\rho = 1.0$–$2.0\,\mathrm{g\,cm^{-3}}$, the lower limit for superficial features is 6–7 km. If material strength may increase toward the nucleus, the surface might support more prominent features. Also, considering the sizes of the structures observed by spacecraft in other objects, assuming features up to 7 km on MS4's surface is reasonable.

The first evidence of topography was observed in the Varages light curve. This data set does not have dead time between the images, and each exposure translates into a resolution of 1.97 km into the sky plane. The Fresnel diffraction and stellar diameter at MS4 geocentric distance are at the same level, 1.54 km and 1.19 km, respectively. The mentioned light curve presents a sharp ingress and a gradual egress above the noise level, as shown in Fig. 4. The feature did not appear in the other high S/N light curves, thus weakening the possibility of a secondary star. Therefore, the most plausible explanation is a topography where a portion of the star appeared a few frames before egress, corresponding to ≈10 km-long feature in the chord's direction. The insert in Fig. 4 displays the stellar position in each frame, represented by yellow circles, relative to a proposed limb in gray.

The second evidence of topography on MS4's observed limb comes when investigating the residuals of the average ellipse presented before. Some groups of points between PA = –5° and PA = 120° presented a large offset regarding the global limb. Therefore, to better describe this local limb, we built a model based on a combination of symmetric parabolas, the simplest function that can reproduce the observed features. Equations (1) and (2) provide the models used to fit the group of points with negative and positive dispersion (R_D), respectively. The y term defines the parabola's depth and height, when positive indicates depression. The x term is related to the parabola's curvature. PA is the position angle, and z accounts for the parabola's distance from the plot's origin. The model's R_D values outside the topography region are defined as being zero.

$$Depression = \begin{cases} 0 & R_D \geq 0, \\ x(\mathrm{PA} - z)^2 - y & R_D < 0. \end{cases} \quad (1)$$

$$Elevation = \begin{cases} 0 & R_D \leq 0, \\ x(\mathrm{PA} - z)^2 + y & R_D > 0. \end{cases} \quad (2)$$

Then, the model is built by summing the equations,
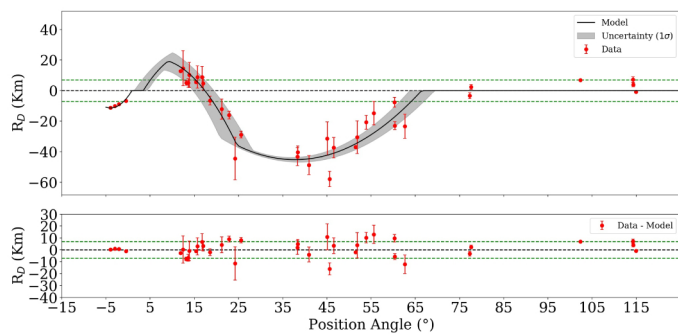
$$Model = Depression + Elevation + Depression,$$

Fig. 5. Limits of the assumed ± 7 km tolerance (see text) shown as horizontal green lines and the black dashed line is the best-fit ellipse. *Upper panel*: red points (R_D) are the distance of each point from the best-fit ellipse (in the normal-to-the-ellipse direction) as a function of the position angle, and the solid black line is the model with 1σ uncertainty represented in gray. *Lower panel*: residuals after subtracting the model from the data points.

where one depression corresponds to the Varages egress region (shown here as negative position angles for better viewing).

The fitting was made using a high-level PYTHON interface named LMFIT[10], designed for non-linear optimization and curve-fitting problems. First, we used the differential evolution (DE) minimization method (Storn and Price 1997) to derive the first estimation of the model's parameters, which can explore large areas of candidate space without getting stuck in a local minimum. Then, to get a representative estimation of the model's uncertainties, we explored the parameter space using the maximum likelihood via Monte Carlo Markov chain sampler: *emcee*[11] (Foreman-Mackey et al. 2013). The center of each feature was limited as follows: main depression between $40° \pm 20°$, elevation between $7.5° \pm 7.5°$, while the Varages depression was fixed on PA $= -3.9°$. The model section between $-5°$ and $0°$ does not have significant errors due to the precision of the grazing detection presented in Fig. 4. For this angle interval, we do not allow the sampler to estimate for unknown uncertainties. However, for the elevation and the main depression, *emcee* found that unknown uncertainties must be about 4.5 km. This value is reasonable, considering that the 7 km of tolerance assumed during the global fit was not included in the points error bars.

After subtracting the model from the data set, residuals are inside the expected range (bottom panel in Fig. 5). Therefore, according to the model at 1σ level, MS4's surface has an ≈ 11 km depth depression in the region detected by Varages station, followed by an elevation of 25^{+4}_{-5} km. However, the most impressive feature is the 45.1 ± 1.5 km depth depression with a linear extension of 322 ± 39 km. Figure 6 presents a general view of the detected limb and summarizes the topography solutions. However, because the depression was likely not in its middle position at the limb, it is likely more extensive and profound than what it seems from this snapshot at a particular rotation phase. Such prominent superficial features may be caused by collisions with other small objects.

3.3. Other occultation events

An object's 3D shape is strongly correlated with the body's rotational modulation (Chandrasekhar 1987; Tancredi and

---

[10] More about this library can be found in the https://lmfit.github.io/lmfit-py/

[11] Documentation available on https://emcee.readthedocs.io/en/stable/
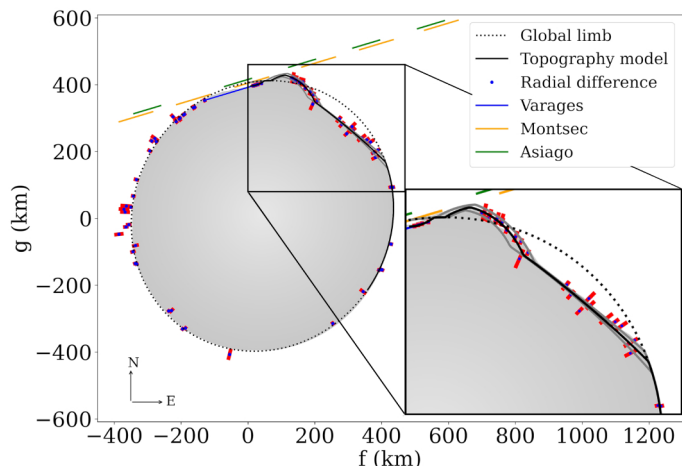
Fig. 6. R_D points projected at the sky plane in blue points, with 1σ uncertainties in red. The blue segment is the positive detection from Varages station. Orange and green segments correspond to negative frames acquired in Montsec and Asiago stations, respectively. In black, the dotted line is the best-fitted global limb model described in Sect. 3.1, and the solid line is the model for local topography. The solid gray lines limit the topographic model's 1σ-error bars. Finally, the filled gray color shows the proposed global limb with topography.

Favre 2008). For example, Maclaurin objects usually have single-peaked rotational light curves with small peak-to-peak amplitudes caused by albedo features. In contrast, the rotational light curve of a Jacobi shape presents double-peaked curves with more pronounced amplitudes (unless they are seen nearly pole-on). Therefore, a reasonable determination of MS4's rotational parameters is crucial to derive an accurate 3D size, shape, albedo, and density.

However, MS4 has crossed a highly dense field of stars since its discovery. Therefore, it is complicated to obtain precise photometric measurements because it is usually blended with faint background stars (as seen from Earth). However, in 2011 it passed in front of a dark cloud when it was observed well isolated from other stars in about 100 images. Using those images along with a data set acquired in the Sierra Nevada observatory, Thirouin (2013) derived a single-peaked light curve with an amplitude of 0.05 ± 0.01 mag and two possibilities for the rotational period: 7.33 h or 10.44 h. Such a small amplitude may indicate that MS4 is a Maclaurin object. It is also possible that it is a triaxial body, such as a Jacobi ellipsoid observed close to a pole-on orientation. Considering the observed small amplitude and small change in the aspect angle, the projected area on the sky plane between 2019 and 2022 should not change considerably. Nevertheless, if it is a triaxial object, the position angle of the projected ellipse on each observed occultation will present significant changes according to its rotational phase.

Due to its large diameter and small rotational light curve amplitude, the Maclaurin spheroid is our preferred 3D shape for MS4. Thus, we tried fitting the same 3σ solution derived from the 8 August 2020 event (Table 4) on the chords obtained on the other occultation events. Using χ^2 minimization, the ellipse was fitted with the center (f and g) as a free parameter. When two center positions are equally possible (single chord cases), we present the center solution closer to the position predicted by the NIMA v9 ephemeris. Figures 7 and 8 show the results of the limb fitting for the other eight events. Table 5 presents the derived astrometric information, and Appendix A shows
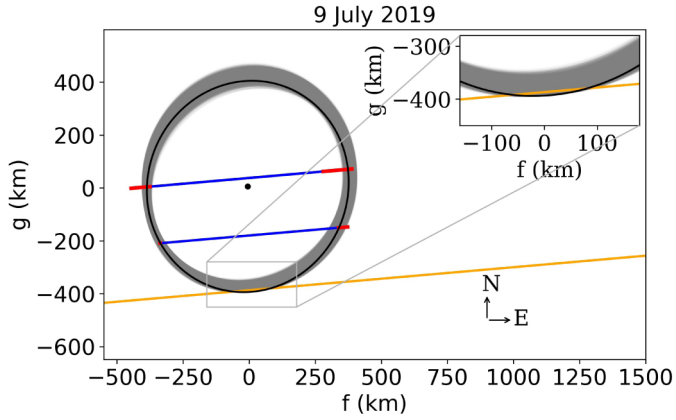
9 July 2019

Fig. 7. Positive data from the stellar occultation on 9 July 2019 shown as the blue segments. The 1σ uncertainties are in red, and the negative chord acquired from the Ponta Grossa station is in orange. The best-fitted ellipse is in black, with the center presented by the black dot, and the solutions in the 3σ range are in gray. The fit considers topographic features up to 7 km in size. Thus, the ellipses crossing the negative chord are in this range.

Table 5. Astrometric information (ICRS) for the geocentric closest approach instant (UT) obtained from the nine stellar occultation events observed between 2019 and 2022, sorted by date (day-month-year).

Date	Instant (UT) (hh:mm:ss.ss)	Right ascension (hh mm ss.ss)	Error (mas)	Declination (° ′ ″)	Error (mas)
09-07-2019	04:23:49.08	18 45 19.245981	0.23	–06 24 13.05928	0.60
26-07-2019	02:47:08.52	18 44 07.573463	0.57	–06 26 40.17686	0.51
26-07-2019	10:18:43.02	18 44 06.315990	0.37	–06 26 43.7686	1.3
19-08-2019	07:41:52.28	18 42 43.51613	1.0	–06 32 33.9776	1.1
26-07-2020	23:17:56.04	18 48 18.075014	0.12	–06 13 31.70897	0.12
08-08-2020	20:44:27.26	18 47 29.961308	0.12	–06 16 31.34442	0.10
24-02-2021	08:45:52.82	18 56 35.9873	1.1	–06 30 23.1583	2.8
14-10-2021	03:26:05.50	18 50 30.768595	0.48	–06 24 13.20676	0.52
10-06-2022	05:32:47.30	19 00 15.446841	0.32	–05 42 42.8843	1.3

the post-occultation maps with the observed shadow path and station locations.

3.4. MS4's size, shape, and albedo

As mentioned previously in this work, we consider MS4 to have a Maclaurin shape ($a = b > c$) with an equatorial radius a, polar radius c, and true oblateness $\epsilon = (a - c)/a$. Given it is a Maclaurin body, the apparent semi-major axis will be equal to the true semi-major axis ($a' = a$). In addition, we assume that it was observed with the same aspect angle θ during all the stellar occultations, which $\theta = 0°$ (resp. 90°) corresponds to a pole-on (resp. equator-on) viewing. The maximum true oblateness that a Maclaurin object can have is $\epsilon \leq 0.417$ (Tancredi and Favre 2008), which gives $c = 234$ km. On the other hand, $c > 387$ km if we consider the $\epsilon = \epsilon' = 0.034$, derived from the occultation, as the lower limit for the object's true oblateness. If the above-mentioned conditions are true, those values for the pole radius can be understood as the minimum and maximum values.

The Maclaurin spheroid formalism (Braga-Ribas et al. 2013) allows us to estimate an object's density from the true oblateness and rotational period. Using the lower limit of true oblateness from the occultation and the two rotational periods in the literature, we obtained an upper limit for global density of 8.0 g cm^{-3}
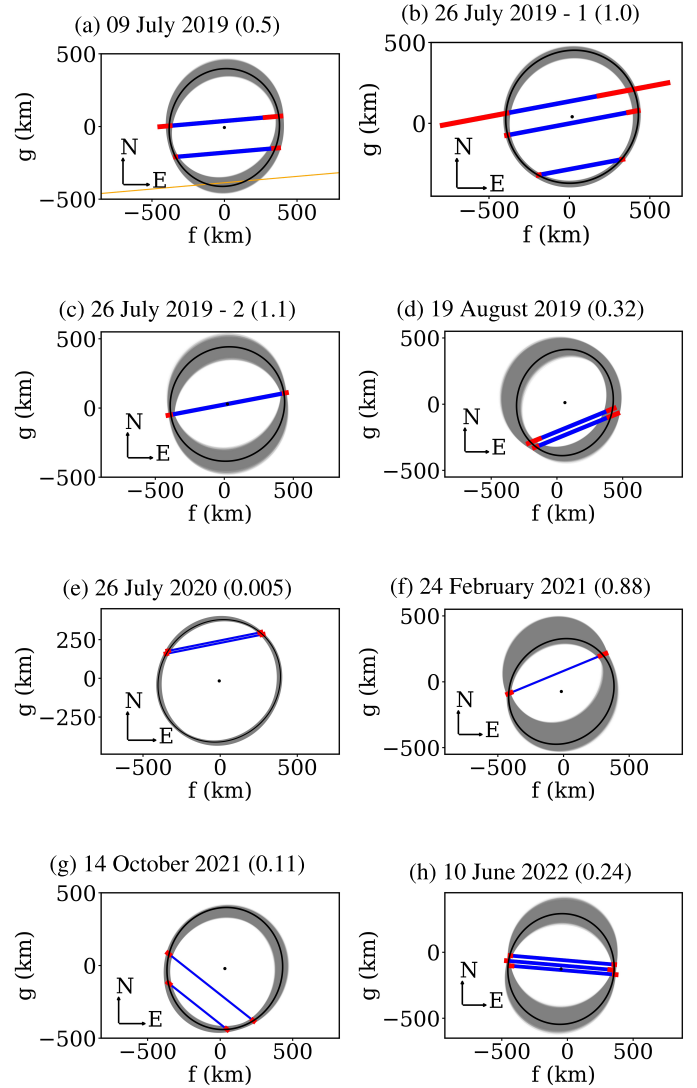
Fig. 8. Results for the additional eight stellar occultation events. Blue segments are the positive detections with 1σ uncertainties in red. The best elliptical limb is in black, with the center presented by the black dot. The gray region presents all the limb solutions within 3σ. The χ^2_{pdf} of each fit is presented between parenthesis in the individual labels. For the occultations presented in d, e, and f, the chosen center solution was the closest one to the predicted by NIMA v9 ephemeris.

and 3.9 g cm^{-3} for periods of 7.33 h and 10.44 h, respectively. These values are too high for objects in the trans-Neptunian region, so it is reasonable to infer that the true oblateness is higher than the observed in the stellar occultation events. As shown in Fig. 9, the density decreases as the true oblateness increases. Therefore, we can use the upper limit for the oblateness of a Maclaurin object ($\epsilon = 0.417$) to obtain the lower limits of MS4's global density, which gives 0.72 g cm^{-3} and 0.36 g cm^{-3} for 7.44 h and 10.44 h, respectively.

Finally, a geometric albedo of $p_V = 0.1 \pm 0.025$ was calculated using the equivalent radius from the occultation and the absolute magnitude on V-band of $H_V = 3.63 \pm 0.05$ mag, which was obtained from the published V-magnitudes by Verbiscer et al. (2022). The obtained absolute magnitude is in agreement with (Tegler et al. 2016). However, we consider the different phase angles of the measurements and the error bar was calculated considering the expected amplitude of the rotational
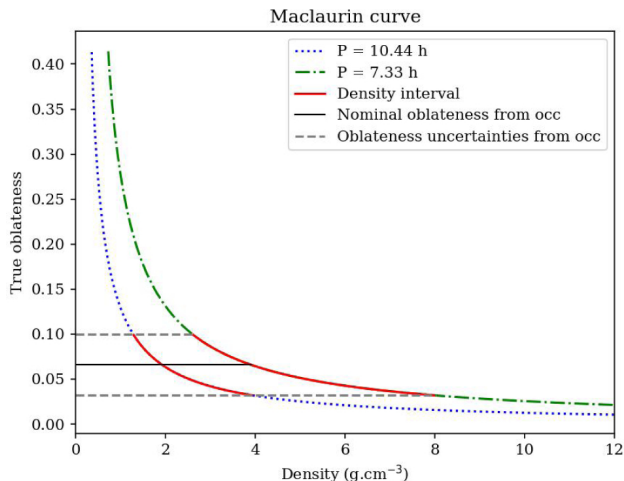
Fig. 9. Relation between the true oblateness and the density of a Maclaurin spheroid for the rotational periods of 10.44 h (blue dotted line) and 7.33 h (green dashed line). The solid black line is the nominal oblateness value with uncertainties (gray dashed lines) derived from the multichord stellar occultation event. Red segments present the global density interval for each rotational period assuming that the apparent oblateness corresponds to the real one.

light curve of $\Delta_m = 0.05$ mag (Thirouin 2013; Thirouin et al. 2013).

4. Discussion and conclusions

This work presents physical and astrometric information derived from nine stellar occultations by the hot classical TNO (307261) 2002 MS$_4$ observed between 2019 and 2022 from South and North America, Africa, Europe, and Western Asia sites. The most successful campaign took place on 8 August 2020, with 116 telescopes involved and 61 positive chords, which represents a record number of detections of a stellar occultation by a TNO up to date.

The projected elliptical limb of MS4 derived from the 8 August 2020 provides a semi-major axis of 412 ± 10 km, a semi-minor axis of 385 ± 17 km, and an area-equivalent radius of 398 ± 12 km. The obtained diameter is ≈ 138 km smaller than that derived with observations in thermal bands (Vilenius et al. 2012). It may indicate the presence of an unknown satellite as suggested for 2002 TC$_{302}$ in similar circumstances (Ortiz et al. 2020a). Still, the error bars from the thermal diameter are large and can accommodate the difference within 3σ.

Despite their being inconclusive, a shallow rotational light curve, the derived equivalent diameter, and the agreement between the limb obtained from the nine stellar occultations favor an oblate spheroid (Maclaurin) for the 3D shape of MS4. Furthermore, considering the expected values for TNOs, the density intervals mentioned above are quite large. This indicates that the object's true oblateness is higher than observed in the occultations or that the observed topography is the cause of the brightness variation in the rotational light curves. In the last case, the real rotational period may be double the published values, which provides smaller densities in the Maclaurin curve (Fig. 9). In any case, more data are needed to confirm MS4's 3D shape and density.

In addition, this work presents the first detailed multichord detection of an extensive feature on the surface of a monolithic TNO. A method was developed to identify and measure

such detection. In the northeast region of the observed limb, a ≈ 11 km depth depression was found, followed by an elevation of 25^{+4}_{-5} km, subsequently followed by the most impressive feature, namely, a 45.1 ± 1.5 km depth depression with a linear extension of 322 ± 39 km. Assuming a straight line that connects the model's initial and endpoints, the largest feature has $\approx 40\%$ of the object's equivalent diameter. Such large topography is out of the range of expected global topography (Sect. 3.2) and may indicate a big impact during MS4 history. If so, one hypothesis that can be raised is whether the impact could have created a collisional family, such as that of Haumea (Brown et al. 2007; Vilenius et al. 2018), the only known collisional family in the trans-Neptunian region.

A comparison can be made with known craters in the outer Solar System. Among the largest Saturnian satellites, the Voyager and Cassini missions were able to acquire images of Tethys and Iapetus. The largest imaged craters are similar in size ratio to the feature observed in MS4. The Odysseus crater has a rim-to-rim diameter corresponding to $\approx 43\%$ of the Tethys's mean diameter. The Turgis[12] crater has a diameter of $\approx 40\%$ Iapetus' mean diameter (Moore et al. 2004; Thomas and Dermott 1991). However, the most recent and detailed studies about the surface of similar-to-MS4 objects in the trans-Neptunian region were performed for the Pluto-Charon system. Contrary to Saturn's satellites, the largest craters imaged by New Horizons have only 10.5% and 18.9% of the Pluto- and Charon-equivalent diameters, respectively (Moore et al. 2016). Therefore, the putative crater on the MS4 limb is the largest observed in the trans-Neptunian region, despite having a similar size ratio to craters found on planetary satellites.

Finally, even with the unprecedented coverage of a stellar occultation by a TNO, no clear secondary drops in the star flux caused by rings, jets, or satellites were identified. Establishing upper limits for detecting such structures in the occultation light curves is beyond the scope of this work. In addition, although it is still very unlikely, we cannot rule out the hypothesis that the elevation observed between PA = 0° and PA = 25° was caused by an unknown satellite with a diameter of ≈ 213 km passing in front of or behind the main body. If so, the main body would then have an effective diameter of ≈ 788 km (see Appendix D).

---

[12] Turgis diameter was obtained from https://planetarynames.wr.usgs.gov/Feature/14488

References

Assafin, M. 2023, Planet. Space Sci., submitted
Assafin, M., Vieira Martins, R., Camargo, J. I. B., et al. 2011, Gaia follow-up network for the Solar System objects: Gaia FUN-SSO workshop proceedings, 85
Astropy Collaboration (Robitaille, T. P., et al.) 2013, A&A, 558, A33
Benecchi, S. D., Porter, S. B., Buie, M., et al. 2019, Icarus, 334, 11
Braga-Ribas, F., Sicardy, B., Ortiz, J. L., et al. 2013, ApJ, 773, 26
Braga-Ribas, F., Crispim, A., Vieira-Martins, et al. 2019, J. Phys. Conf. Ser., 1365, 012024
Brown, M. E., Barkume, K. M., Ragozzine, D., et al. 2007, Nature, 446, 294
Buie, M. W., Porter, S. B., Tamblyn, P., et al. 2020, AJ, 159, 130
Butcher, H., & Stevens, R. 1981, Kitt Peak Natl. Observatory Newslett., 16, 6
Chandrasekhar, S. 1987, Ellipsoidal figures of equilibrium (New York: Dover)

Coppejans, R., Gulbis, A. A. S., Kotze, et al. 2013, PASP, 125, 976
Desmars, J. 2015, A&A, 575, A53
Desmars, J., Camargo, J. I. B., Braga-Ribas, F., et al. 2015, A&A, 584, A96
Dias-Oliveira, A., Sicardy, B., Ortiz, J. L., et al. 2017, AJ, 154, 22
Foreman-Mackey, D., Hogg, D. W., Lang, D., et al. 2013, PASP, 125, 306
Gaia Collaboration (Prust, T., et al.) 2016a, A&A, 595, A1
Gaia Collaboration (Brown, A. G. A., et al.) 2016b, A&A, 595, A2
Gaia Collaboration (Brown, A. G. A., et al.) 2018, A&A, 616, A1
Gaia Collaboration (Vallenari, A., et al.) 2023, A&A, 674, A1
Gladman, B., Marsden, B. G., & Vanlaerhoven, C. 2008, The Solar System Beyond Neptune, eds. M. A. Barucci, H. Boehnhardt, D. P. Cruikshank, & A. Morbidelli (University of Arizona Press, Tucson), 43
Gomes-Júnior, A. R., Morgado, B. E., Benedetti-Rossi, G., et al. 2022, MNRAS, 511, 1167
Jewitt, D., & Luu, J. 1993, Nature, 362, 730
Jewitt, D., Morbidelli, A., & Rauer, H. 2008, Saas-Fee Advanced Course 35: Trans-Neptunian Objects and Comets (Springer Berlin, Heidelberg)
Johnson, T. V., & McGetchin, T. R. 1973, Icarus, 18, 612
Kervella, P., Thévenin, F., Di Folco, E., et al. 2004, A&A, 426, 297
Kilic, Y., Braga-Ribas, F., Kaplan, M., et al. 2022, MNRAS, 515, 1346
Lacerda, P., Fornasier, S., Lellouch, E., et al. 2014, ApJ, 793, L2
Leiva, R., Sicardy, B., Camargo, J. I. B., et al. 2017, AJ, 154, 159
Lellouch, E., Santos-Sanz, P., Lacerda, P., et al. 2013, A&A, 557, A60
Loveless, S., Prialnik, D., & Podolak, M. 2022, ApJ, 927, 178
Moore, J. M., Schenk, P. M., Bruesch, L. S., et al. 2004, Icarus, 171, 421
Moore, J. M., McKinnon, W. B., Spencer, J. R., et al. 2016, Science, 351, 1284
Morbidelli, A., Levison, H. F., & Gomes, R. 2008, The Solar System Beyond Neptune, 275
Müller, T., Lellouch, E., & Fornasier, S. 2020, The Trans-Neptunian Solar System, 153
Nesvorný, D., & Morbidelli, A. 2012, AJ, 144, 117
Nimmo, F., Umurhan, O., Lisse, C. M., et al. 2017, Icarus, 287, 12
Ortiz, J. L., Santos-Sanz, P., Sicardy, B., et al. 2020a, A&A, 639, A134
Ortiz, J. L., Sicardy, B., Camargo, J. I. B., et al. 2020b, The Trans-Neptunian Solar System, 413
Pavlov, H., Anderson, R., Barry, T., et al. 2020, J. Occult. Astron., 10, 8
Petit, J.-M., Kavelaars, J. J., Gladman, B., & Loredo, T. 2008, The Solar System Beyond Neptune, 71
Schenk, P. M., & Moore, J. M. 2020, Philos. Trans. Roy. Soc. Lond. A, 378, 20200102
Spencer, J. R., Stern, S. A., Moore, J. M., et al. 2020a, Science, 367, aay3999
Spencer, J., Grundy, W. M., Nimmo, F., et al. 2020b, The Trans-Neptunian Solar System, 271
Stansberry, J., Grundy, W., Brown, M., et al. 2008, The Solar System Beyond Neptune, 161
Stern, S. A., Bagenal, F., Ennico, K., et al. 2015, Science, 350, aad1815
Stern, S. A., Weaver, H. A., Spencer, J. R., et al. 2019, Science, 364, aaw9771
Stern, S. A., Spencer, J. R., Verbiscer, A., et al. 2020, The Trans-Neptunian Solar System, 379
Storn, R., & Price, K. 1997, Differential Evolution -- A Simple and Efficient Heuristic for global Optimization over Continuous Spaces, 11
Tancredi, G., & Favre, S. 2008, Icarus, 195, 851
Tegler, S. C., Romanishin, W., Consolmagno, G. J., et al. 2016, AJ, 152, 210
Thirouin, A. 2013, PhD. Thesis, University of Granada, Spain
Thirouin, A., Noll, K. S., Campo Bagatin, A., Ortiz Moreno, J. L., & Morales, N. 2013, AAS, DPS Meeting Abstracts 45, 507.04
Thomas, P. C., & Dermott, S. F. 1991, Icarus, 94, 391
Van Laerhoven, C., Gladman, B., Volk, K., et al. 2019, AJ, 158, 49
Verbiscer, A. J., Helfenstein, P., Porter, S. B., et al. 2022, Planet. Sci. J., 3, 95
Vilenius, E., Kiss, C., Mommert, M., et al. 2012, A&A, 541, A94
Vilenius, E., Stansberry, J., Müller, T., et al. 2018, A&A, 618, A136
Weaver, H. A., & Stern, S. A. 2008, The Solar System Beyond Neptune, 557

[1] National Observatory/MCTI, R. General José Cristino 77, CEP20921-400, Rio de Janeiro, Brazil
e-mail: flaviarommel@on.br
[2] Interinstitutional e-Astronomy Laboratory – LIneA & INCT do e-Universo, Rio de Janeiro, Brazil
[3] Federal University of Technology – Paraná (PPGFA/UTFPR – Curitiba), Av. Sete de Setembro 3165, Curitiba, Paraná, Brazil
[4] Institute of Astrophysics of Andalucía, IAA-CSIC, Glorieta de la Astronomía s/n, 18008 Granada, Spain
[5] LESIA, Paris Observatory, PSL University, CNRS, Sorbonne University, Univ. Paris Diderot, Sorbonne Paris Cité, 5 place Jules Janssen, 92195 Meudon, France

[6] Polytechnic Institute of Advanced Sciences-IPSA, 63 boulevard de Brandebourg, 94200 Ivry-sur-Seine, France

[7] Institute of Celestial Mechanics and Ephemeris Calculation (IMCCE), Paris Observatory, PSL Research University, CNRS, Sorbonne University, UPMC Univ Paris 06, Univ. Lille, 77, Av. Denfert-Rochereau, 75014 Paris, France

[8] Valongo Observatory, Federal University of Rio de Janeiro (UFRJ), Ladeira Pedro Antônio 43 – Saúde, 20080-090 Rio de Janeiro, Brazil

[9] Orbital Dynamics and Planetology Group, São Paulo State University (UNESP), Av. Ariberto Pereira da Cunha 333, Guaratinguetá, 12516-410 São Paulo, Brazil

[10] Institute of Physics, Federal University of Uberlândia, Uberlândia, Minas Gerais, Brazil

[11] Florida Space Institute, University of Central Florida, 12354 Research Parkway, Partnership 1, Orlando, Florida, USA

[12] Space Telescope Science Institute, 3700 San Martin Drive, Baltimore, Maryland, USA

[13] Department of Astronomy, and of Earth and Planetary Science, 501, Campbell Hall, University of California, Berkeley, CA 94720, USA

[14] naXys, Department of Mathematics, University of Namur, Rue de Bruxelles 61, 5000 Namur, Belgium

[15] Domaine de la Blaque Observatory, Domaine de la Blaque, 83670 Varages, France

[16] San Pedro de Atacama Celestial Explorations (SPACE), Chicache 81, Ayllu de Solor, 1410000 San Pedro de Atacama, Chile

[17] Panamanian Observatory in San Pedro de Atacama (OPSPA), Chile

[18] Anarchist Mt. Observatory, British Columbia V0H1V6, Canada

[19] STAR Institute, University of Liège, Allée du 6 aoûtl 19C, 4000 Liège, Belgium

[20] Côte d'Azur University, CNRS, Observatoire de la Côte d'Azur, IRD, Géoazur, 250 rue Albert Einstein, Sophia Antipolis 06560 Valbonne, France

[21] Côte d'Azur Observatory, Géoazur UMR 7329, 2130 Route de l'Observatoire, 06460 Caussols, France

[22] University of Zagreb, Faculty of Electrical Engineering and Computing, Department of Applied Physics, Unska 3, 10000 Zagreb, Croatia

[23] Centro Astronómico Hispano en Andalucía, Observatorio de Calar Alto, Sierra de los Filabres, 04550 Gérgal, Spain

[24] Hvar Observatory, Faculty of Geodesy, University of Zagreb, Kačićeva 26, 10000 Zagreb, Croatia

[25] Gemini Observatory/NSF's NOIRLab, Casilla 603, La Serena, Chile

[26] Konkoly Observatory, Research Centre for Astronomy and Earth Sciences (ELKH), Konkoly Thege Miklos út 15–17, 1121 Budapest, Hungary

[27] CSFK, MTA Centre of Excellence, Konkoly Thege Miklós út 15–17, 1121 Budapest, Hungary

[28] Algiers Observatory, CRAAG, Route de l'Observatoire, Algiers, Algeria

[29] Odesa I. I. Mechnikov National University, Astronomical Observatory, Marazliivska 1v, 65014 Odesa, Ukraine

[30] Main astronomical observatory of National Academy of Sciences of Ukraine, 27 Akademika Zabolotnoho St., 03143 Kyiv, Ukraine

[31] Department of Astronomy and Space Sciences, Faculty of Science, Istanbul University, 34116 Istanbul, Turkey

[32] Istanbul University Observatory Research and Application Center, 34116 Istanbul, Turkey

[33] Research Centre for Astronomy, Astrophysics and Astrophotonics, Department of Physics and Astronomy, Macquarie University, 2109 Sydney, Australia

[34] ARC Centre of Excellence for All-Sky Astrophysics in 3 Dimensions, Stromlo, Australian Capital Territory, Australia

[35] Çanakkale Onsekiz Mart University, School of Graduate Studies, Department of Physics, 17100 Çanakkale, Turkey

[36] Çanakkale Onsekiz Mart University, Astrophysics Research Center and Ulupınar Observatory, 17100 Çanakkale, Turkey

[37] International Occultation Timing Association – European Section (IOTA-ES), Am Brombeerhag 13, 30459 Hannover, Germany

[38] Sabadell Astronomical Association, Carrer Prat de la Riba, s/n, 08206 Sabadell, Catalonia, Spain

[39] PSTJ astronomy club – CIV 190 Rue Frédéric Mistral, 06560 Valbonne, France

[40] British Astronomical Association (BAA), 25 Farringdon Street, London EC4A 4AB, UK

[41] AstroCampania Association, Via Servio Tullio n. 101, 80126 Naples, Italy

[42] Instituto de Física Aplicada a las Ciencias y las Tecnologías, Alicante University, San Vicente del Raspeig, 03080 Alicante, Spain

[43] Institut de Ciències del Cosmos (ICCUB), Barcelona University (IEEC-UB), Carrer de Martí i Franquès 1, 08028 Barcelona, Spain

[44] Ponta Grossa State University, Av. Carlos Cavalcanti 4748, Ponta Grossa, Paraná, Brazil

[45] Department of Earth, Atmospheric and Planetary Science, Massachusetts Institute of Technology, 77 Massachusetts Avenue, Cambridge, MA, USA

[46] Astrobiology Research Unit, University of Liège, Allée du 6 août 19C, 4000 Liège, Belgium

[47] Canary Islands Institute of Astrophysics (IAC), Vía Láctea s/n, 38205 La Laguna, Tenerife, Spain

[48] INAF – Catania Astrophysical Observatory, via S. Sofia 78, 95123 Catania, Italy

[49] Campo Catino Astronomical Observatory, Località Colle Pannunzio, 03016 Guarcino (FR), Italy

[50] Institute of Astronomy of V.N. Karazin Kharkiv National University, Kharkiv 61022, Sumska str. 35, Ukraine

[51] Astronomical Observatory Institute, Faculty of Physics, Adam Mickiewicz University, Słoneczna 36, 60-286 Poznań, Poland

[52] Crni Vrh Observatory, Predgriže 29A, 5274 Crni Vrh nad Idrijo, Slovenia

[53] University of Ljubljana, Faculty of Mathematics and Physics, Jadranska 19, 1000 Ljubljana, Slovenia

[54] Pistoiese Mountain Astronomical Observatory (GAMP), San Marcello Pistoiese, Italy

[55] Astronomical Association of Eivissa (AAE), Lucio Oculacio 29, 07800 Ibiza, Spain

[56] Monte Agliale Astronomical Observatory, Via Cune Motrone, 55023 Borgo a Mozzano, Italy

[57] QOS Observatory, Center for Special Information Reception and Processing and Navigation Field Control, National Space Facilities Control and Test Center, Zalistsi village, 32444 Kamianets-Podilskyi district, Khmelnytskyi region, Ukraine

[58] La Laguna University (ULL), Astrophysics department, Avenida Astrofísico Francisco Sánchez, s/n, Facultad de Ciencias, Sección de Física, 38200 La Laguna, Tenerife, Spain

[59] Virtual Telescope Project, Via Madonna de Loco 47, 03023 Ceccano, Italy

[60] G. Pascoli Observatory (MPC K63), Via dei Pieri 1, 55051 Castelvecchio Pascoli, Italy

[61] Red ASTRONAVARRA sarea, 25250 Bellpuig, Catalunha, Spain

[62] Club Astrospace Thales Alenia Space, 5 Allée des Gabians BP 99, 06156 Cannes, France

[63] University of Lille, Lille Observatory, 1 impasse de l'observatoire, 59000 Lille, France

[64] Tavolaia Observatory (MPC A29), Via Tavolaia, 4, 56020 Santa Maria a Monte, Pisa, Italy

[65] Romanian Society for Cultural Astronomy – SRPAC, Coriolan Baran st., 300238 Timisoara, Romania

[66] EPT Observatories, Camino El Pinar, 114, 38780 Tijarafe, Spain

[67] Penticton Secondary School, 158 Eckhardt Ave East Penticton, British Columbia, Canada

[68] OACM Observatory, Fuensanta de Martos, pueblo de Jaen, Spain

[69] Associazione Astrofili Fiorentini (A.A.F.) – Via Giulio Caccini 13b, 50141 Firenze, Italy

[70] Astronomical Society of Southern Africa, Centurion, South Africa

[71] Nastro Verde Astronomical Observatory, Via Nastro Verde 50, Sorrento, Italy

[72] Cosmos Observatory, Calle Cardenal Pedro Gonzalez, 29604 Marbella, Spain

[73] INAF – Trieste Astrophysical Observatory, via G. B. Tiepolo 11, 34143 Trieste, Italy

[74] Lowell Observatory, 1400 Mars Hill Road, Flagstaff, 86001-4470 Arizona, USA

[75] ROASTERR – 1 Observatory, Cluj-Napoca, Romania

[76] PS Observatory (MPC M35), Parjol, Bacau county, Bacau, Romania

[77] The American Association of Variable Star Observers (AAVSO), 185 Alewife Brook Parkway, Suite 410, Cambridge, MA 02138, USA

[78] ALMO Observatory via Forlai 14/C, 40010 Sala Bolognese, Bologna, Italy

[79] UAI (Union of Italian Amateur Astronomers) c/o Osservatorio Astronomico "F. Fuligni" Via Lazio 14, 00040 Rocca di Papa, Roma, Italy

[80] Telescope Live, 71–75 Shelton Street, Covent Garden, London WC2H 9JQ, UK

[81] Bucharest Astroclub, Bd. Lascar Catargiu 21, 010662 Bucharest, Romania

[82] Astronomical society of Tunisia (SAT), physics department, faculty of science of Tunis, Campus universitaire, 2092, El Manar, Tunis, Tunisia

[83] University of Tunis El Manar, University Campus Farhat Hached B.P. 94 Rommana, 1068 Tunis, Tunisia

[84] Ad Astra Sangos Observatory (MPC Z07), Calle Hernán Cortés 4, Alhendín, Granada, Spain

[85] Sociedad Astronómica Granadina, Avenida de Barcelona 20, 10C, 18006 Granada, Spain

[86] Stardust Observatory, 3 Alexandru cel Bu, 500260 Brasov, Romania

[87] Bârlad Astronomical Observatory, Republicii Street 235, 731070 Bârlad, Vaslui County, Romania

[88] Astronomical Institute of the Romanian Academy, Bucharest, 5 Cuţitul de Argint, 040557 Bucharest, Romania

[89] Mississippi State University, 295 Lee Blvd Mississippi State, MS 39762, USA

[90] 113 Kentucky Ave SW, Orange City, Iowa 51041, USA

[91] Syrma-GUA, Paseo de Belén, 9, 47011 Valladolid, Spain

[92] Department of Space Sciences and Technologies, Akdeniz University, Campus, Antalya 07058, Turkey

[93] TÜBİTAK National Observatory, Akdeniz University Campus, Antalya 07058, Turkey

[94] Euraster, 8 rue du tonnelier, 46100 Faycelles, France

[95] IRAP, Midi-Pyrenees Observatory, CNRS, University of Toulouse, BP 4346, 31028 Toulouse Cedex 04, France

[96] Dax Observatory, rue Pascal Lafitte, 40100 Dax, France

[97] El Leoncito Astronomical Complex, National Council for Scientific and Technical Research, San Juan, Argentina

[98] National University of La Plata, Facultad de Ciencias Astronómicas y Geofísicas, Paseo del Bosque s/n, B1900FWA, La Plata, Argentina

[99] National University of La Plata, Instituto de Astrofísica de La Plata (CCT La Plata – CONICET/UNLP), B1900FWA La Plata, Argentina

[100] University Observatory, Ludwig-Maximilians, Munich University, Scheiner Str. 1, 81679 Munich, Germany

[101] Astronomical Institute, Slovak Academy of Sciences, 05960 Tatranská Lomnica, Slovakia

[102] G. V. Schiaparelli Astronomical Observatory, Campo dei Fiori, Varese, Italy

[103] Hieronymusstr. 15b, 81241 Munich, Germany

[104] National Astrophiscs Institute, Padova Astronomical Observatory, Vicolo dell'Osservatorio 5, 35122 Padova, Italy

[105] Aix Marseille University, CNRS, CNES, LAM, Marseille, 13007, France

[106] Astronomical Institute of the Czech Academy of Sciences, Fričova 1, 25165 Ondřejov, Czech Republic

[107] Adiyaman University, Department of Physics, 02040 Adiyaman, Turkey

[108] Astrophysics Application and Research Center, Adiyaman University, Adiyaman 02040, Turkey

[109] Ataturk University, Department of Astronomy and Space Science, Yakutiye, 25240, Erzurum, Turkey

[110] Max-Planck-Institut für extraterrestrische Physik, Giessenbachstrasse, 85748 Garching, Germany

[111] Sybilla Technologies, Torunska 59, 85-023 Bydgoszcz, Poland

[112] Mt. Suhora Observatory, Pedagogical University of Cracow, Podchorazych 2, 30-086 Cracow, Poland

[113] Polytechnic Institute of Tomar, Ci2–Smart Cities Research Center and Unidade Departamental de Matemática e Física (UDMF), 2300 Tomar, Portugal

[114] Aristotle University of Thessaloniki (AUTh), University Campus, 54124 Thessaloniki, Greece

[115] Centro Ciência Viva de Constância-Parque de Astronomia, Alto de Santa Bárbara, Via Galileu Galilei 817, 2250-100 Constância, Portugal

[116] Bülach Observatory (MPC 167), Schul- und Volkssternwarte Bülach, Postfach 540, 8180 Bülach, Switzerland

[117] Stellar Occultation Timing Association Switzerland (SOTAS), Swiss Astronomical Society, Schweizerische Astronomische Gesellschaft SAG-SAS, Fachgruppe Sternbedeckungen/SOTAS, 8200 Schaffhausen, Switzerland

[118] Türksat Observatory – Türksat Company Headquarters Campus, Yaglipinar Mahallesi Türksat (Küme Evler) İdari Bina Apt. No:1, Gölbaşı, Ankara, Turkey

[119] Çukurova University, Department of Astronomy and Astrophysics, Çukurova Üniversitesi Rektörlüğü, 01330 Sarıçam/Adana, Turkey

[120] Adana Yuregir Science Center and Mesopotamia Astronomy Association, Adana, Turkey

[121] Teplice Observatory, North-Bohemian Observatory and Planetarium in Teplice, Koperníkova 3062, 41501 Teplice, Czech Republic

[122] EUR ING, Hviezdoslavova 1971, 022 01 Čadca, Slovakia

[123] GiaGa Observatory, 20005 Pogliano Milanese, Milan, Italy

[124] Filzi School, Passaggio Maria Damian 20, 39055 Laives, Italy

[125] Amateur Astronomical Observatory of Seysses, 700 chemin du Fourtané, 31600 Seysses, France

[126] The Pleiades Latrape Observatory, Grand Rue, 31310 Latrape, France

[127] Herne Observatory, Am Böckenbusch 2a, 44652 Herne, Germany

[128] Board of Polish Amateur Astronomers Society, Krakow, Poland

[129] Polish Astronomical Society, Warsaw, Poland

[130] ul. Krokusowa 6, 16-001 Księżyno, Poland

[131] French Astronomical Society (SAF), 3 rue Beethoven, 75016 Paris, France

[132] KYSUCE Observatory (MPC G02), Kysucke Nove Mesto, Slovakia

[133] Czech Astronomical Society, Fričova 298, 251 65 Ondřejov, Czech Republic

[134] Observatory in Rokycany and Pilsen, Voldušská 721, 33701 Rokycany, Czech Republic

[135] ADAGIO Association, Belesta Observatory (MPC A05), 550 route des étoiles, 31540 Bélesta en Lauragais, Toulouse, France

[136] El Gato Gris Astronomical Observatory (MPC I19), Tanti, 5013 Córdoba City, Argentina

[137] Grupo de Observadores de Rotaciones de Asteroides (GORA), 5013 Córdoba City, Argentina

[138] Proyecto de Observación Colaborativa y Regional de Ocultaciones Asteroidales (POCROA), 5013 Córdoba City, Argentina

[139] El Catalejo Observatory (MPC I48), 6300 Santa Rosa, La Pampa, Argentina

[140] Planetary Science Institute, 1700 East Fort Lowell Road, Suite 106, Tucson, AZ 85719, USA

[141] Applied Physics, Bilbao School of Engineering, University of País Vasco, UPV/EHU, Bilbao, Spain

[142] University of Oregon, Department of Physics, 120 Willamette Hall, 1371 E 13th Avenue Eugene, OR, USA

[143] Purdue University Northwest, Department of Chemistry and Physics, 2200 169th St Hammond, IN 46323, USA

[144] Vasile Urseanu Observatory (MPC A92), 21 Lascar Catargiu, 010662 Bucharest, Romania

[145] Eskişehir Technical University, Observatory on Yunusemre Campus Science Faculty, Physics Department, 26470, Tepebaşı Eskişehir, Turkey

[146] Section of Astrophysics, Astronomy and Mechanics, Department of Physics, National and Kapodistrian University of Athens, 15784 Zografos, Athens, Greece

[147] Institut für Astronomie und Astrophysik, Eberhard Karls Universität Tübingen, Auf der Morgenstelle 10, 72076 Tübingen, Germany

[148] Ondokuz Mayıs University Observatory, Kurupelit Campus, 55139 Atakum, Samsun, Turkey

[149] Institute of Space Sciences (CSIC-IEEC), Campus UAB, Carrer de Can Magrans s/n, 08193 Cerdanyola del Vallès, Catalonia, Spain

[150] Sparta Astronomy Association, 22 Amyklon str., 152 31 Halandri, Greece

[151] NOAK Observatory (MPC L02), Ioannina, Stavraki Delfon 2, 45500, Greece

[152] Department of Physics, University of Ioannina, Ioannina 45110, Greece

[153] g-ral Gheorghe Magheru Blvd, no.7, sc.1, ap. 4, Sector 1, Bucharest, 010322, Romania

[154] Los Cabezones Observatory (MPC X12), Santa Rosa, La Pampa, Argentina

[155] University of Idaho, Department of Physics, Stop 440903, Moscow, ID 83843, USA

[156] Department of Space Studies, University of North Dakota, 4149 University Avenue Stop 9008, Grand Forks, ND 58202-9008, USA

[157] Chagrin Valley Astronomical Society, 15701 Huntley Rd, Huntsburg, OH 44046, USA

[158] Astronomy Department, University of Chile, Camino del Observatorio 1515, Casilla 36-D, Las Condes, Santiago, Chile

[159] Centro de Excelencia en Astrofísica y Tecnologías Afines (CATA), Chile

[160] Millenium Institute of Astrophysics (MAS), Vicuña Mackenna 4860, 7820436 Macul, Santiago, Chile

[161] Institute of Space Science, 409 Atomistilor Street Magurele, 077125 Ilfov, Romania

[162] Squirrel Valley Observatory (MPC W34), 3870 River Rd., Columbus, NC 28722, USA

[163] Department of Physics and Astronomy, University of North Carolina Asheville, 1 University Heights, Asheville, NC 28804, USA

Appendix A: Post occultation maps with sites location

Here, we present the post-occultation maps of each stellar occultation by 2002 MS4 described in this work.
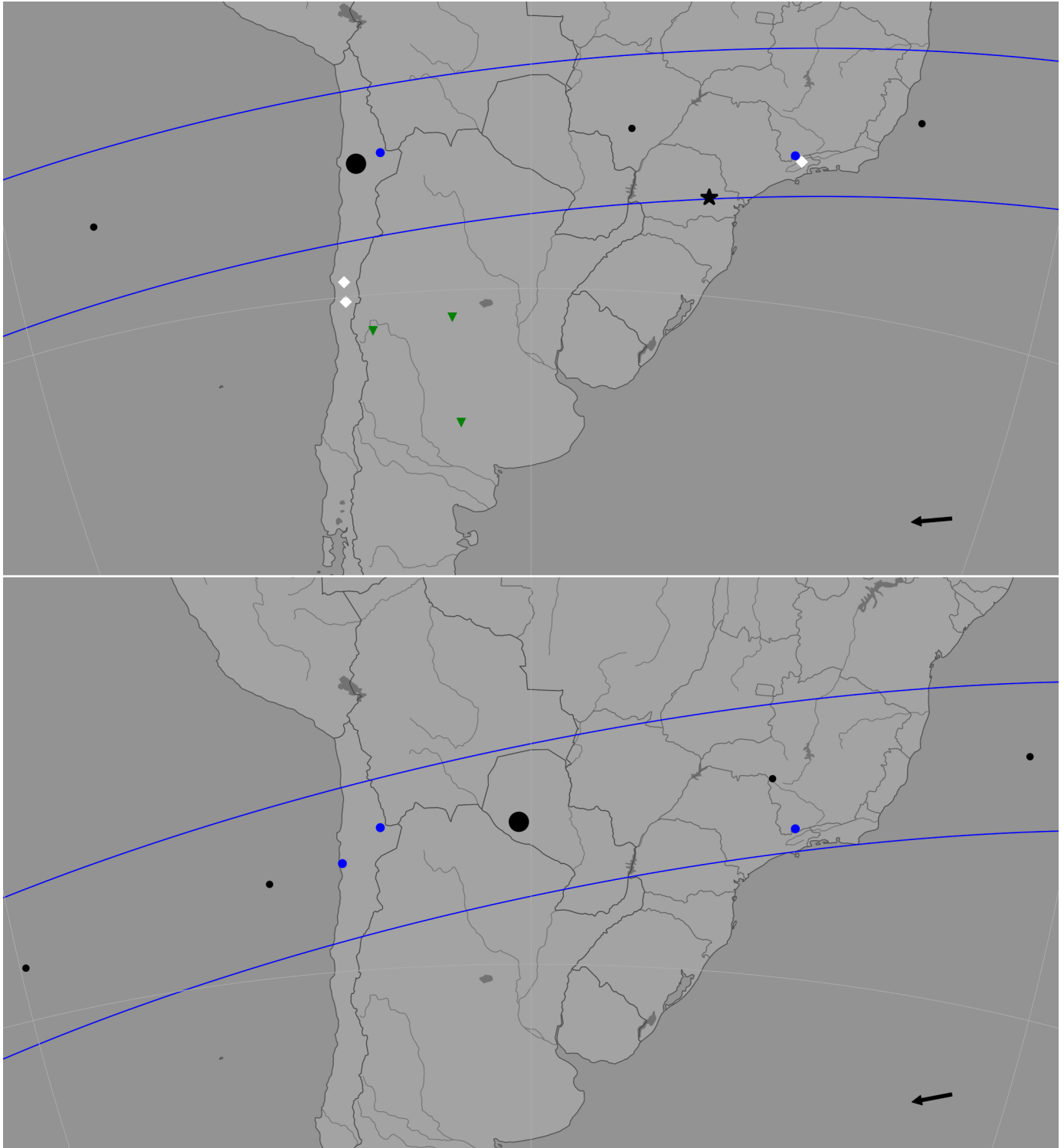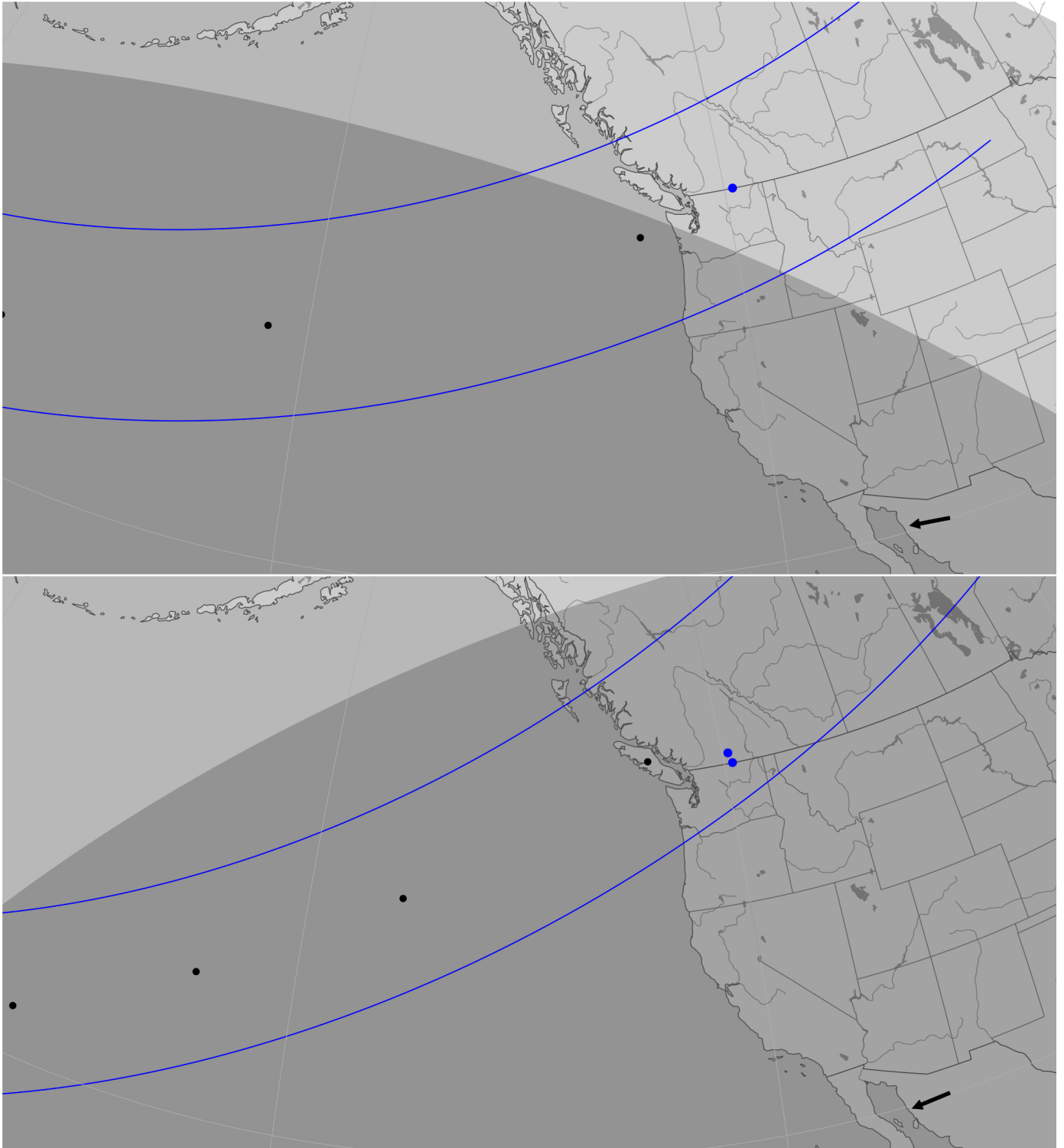

Fig. A.1: Post-occultation map of the stellar occultations observed on July 09 (upper panel) and July 26, 2019 (lower panel) from South America. Solid blue lines and black dots indicate the observed shadow path every minute, and the largest black bullet represents the closest approach instant. The arrow shows the shadow direction over the Earth's surface. Blue dots show the positive detections, green triangles show the negatives and white diamonds show the stations with bad weather conditions or technical problems. The black star marks the Ponta Grossa station, a close negative chord that limits the ellipse solutions at the south for the July 09, 2019, event.

Fig. A.2: Post-occultation map of the stellar occultations observed on July 26 (upper panel) and August 19, 2019 (lower panel) from North America. Solid blue lines and black dots indicate the observed shadow path every minute. The arrow shows the shadow direction over the Earth's surface, and the blue dots show the positive detections.
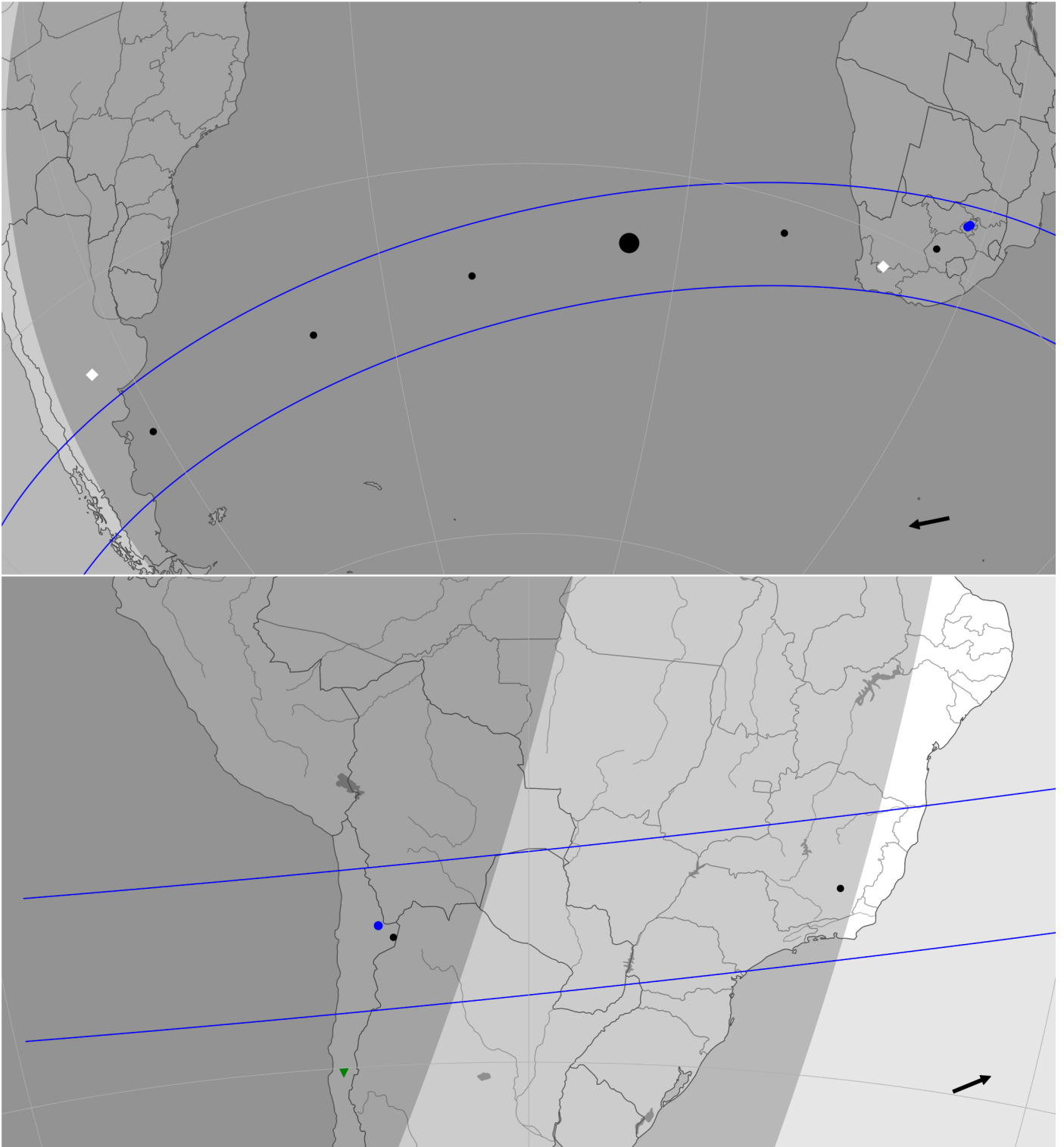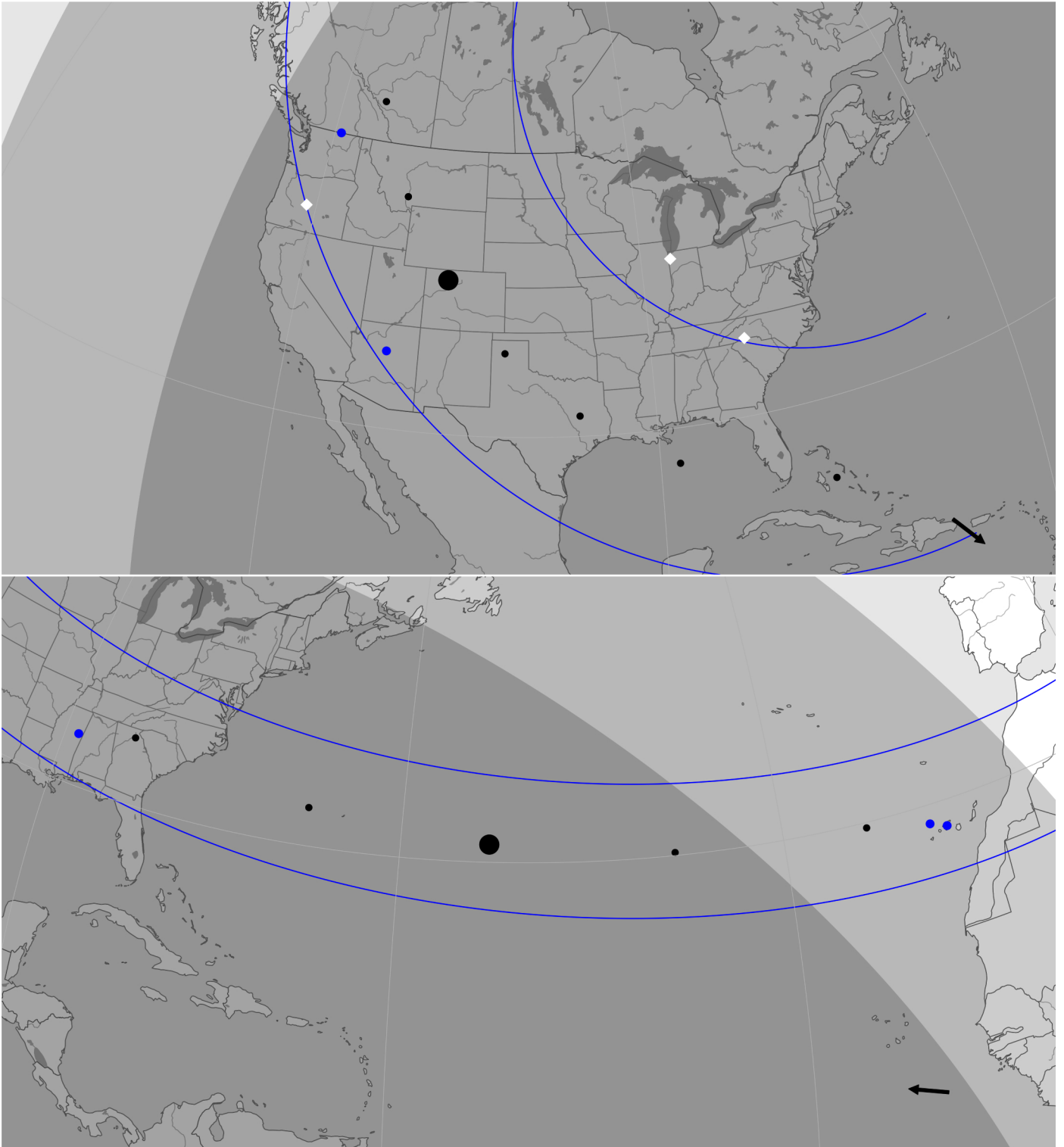
Fig. A.3: Post-occultation map of the stellar occultations observed on July 26, 2020, from South Africa and South America (upper panel) and on February 24, 2021, also from South America (lower panel). Solid blue lines and black dots indicate the observed shadow path every minute, and the largest black bullet represents the closest approach instant. The arrow shows the shadow direction over the Earth's surface. Blue dots show the positive detections, green triangles show the negatives and white diamonds show the stations with bad weather conditions or technical problems.

Fig. A.4: Post-occultation map of the stellar occultations observed on October 14, 2021, from North America (upper panel) and on June 10, 2022, from North America and Europe (lower panel). Solid blue lines and black dots indicate the observed shadow path every minute, and the largest black bullet represents the closest approach instant. The arrow shows the shadow direction over the Earth's surface. Blue dots show the positive detections and white diamonds show the stations with bad weather conditions or technical problems.

Appendix B: Observational circumstances

Tables B.1 to B.5, available at the CDS, summarize the observational circumstances of each station of the nine stellar occultations presented in this work. For better visualization, the tables are divided into two groups: (i) the 8 August 2020 event and (ii) the other eight stellar occultations. The positive, negative, and overcast locations involved in the 8 August 2020 campaign are listed in Tables B.1, B.2, and B.3, respectively. Positive and negative observations of the other eight events are present in Tables B.4 and B.5, respectively.

Appendix C: Light curves

Here, we provide the plots of the 77 positive occultation light curves acquired during the nine events observed between 2019 and 2022. They are normalized to the unity, and the time is given in seconds, counting from 00:00:00 (UTC) of the event date. Figure C.1 presents the plots from the 8 August 2020 stellar occultation, listed from the northernmost to the southernmost stations (on each column). Figure C.2 shows the light curves from the other eight events. The black dots present the observational data and the red line is the fitted model.
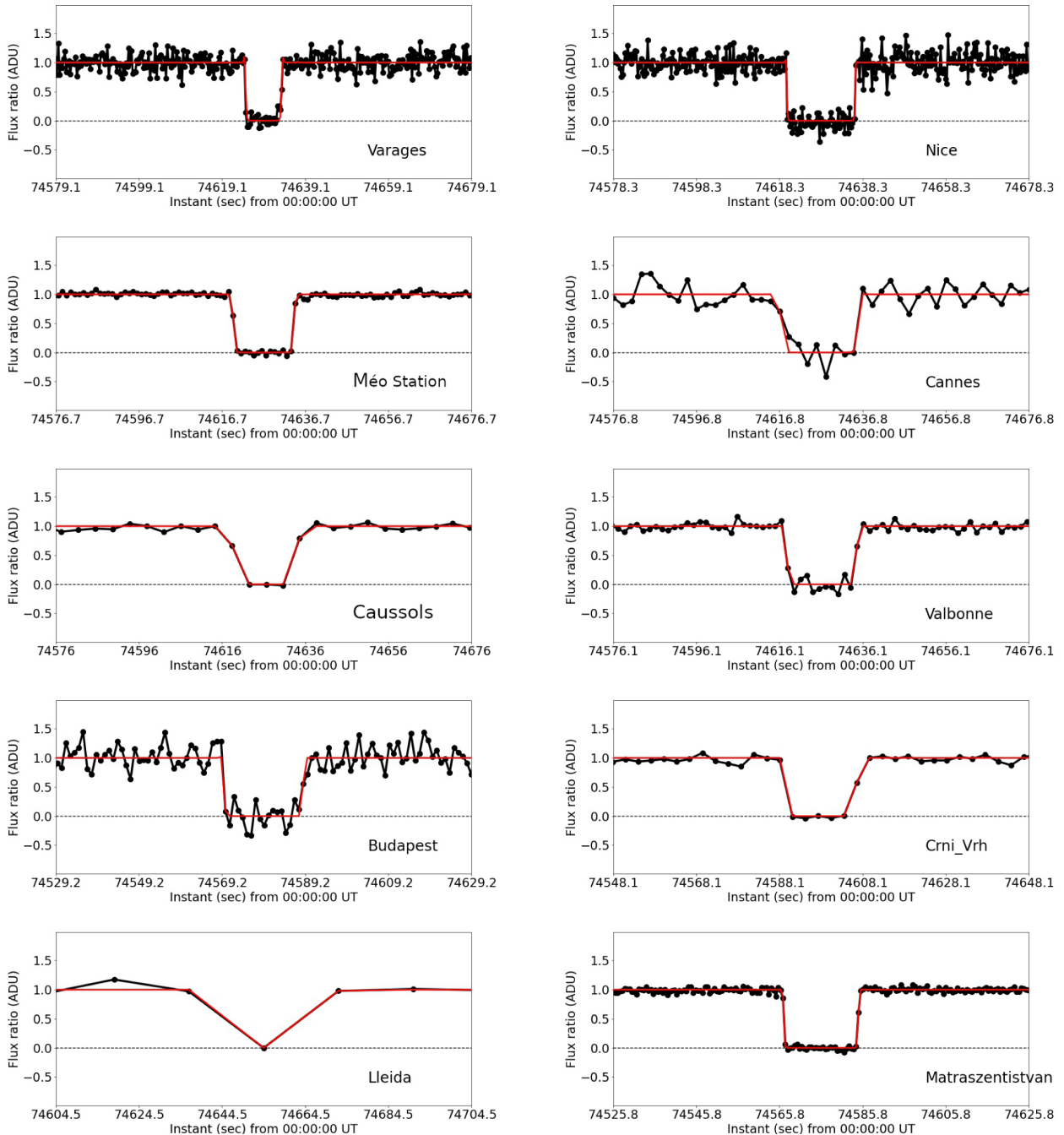

Fig. C.1: Fifty-eight normalized light curves, centered in the occultation instant, obtained on the 8 August 2020 campaign. The station that acquired the light curve is mentioned in each plot. The black and red points present the observed data and the fitted model, respectively.
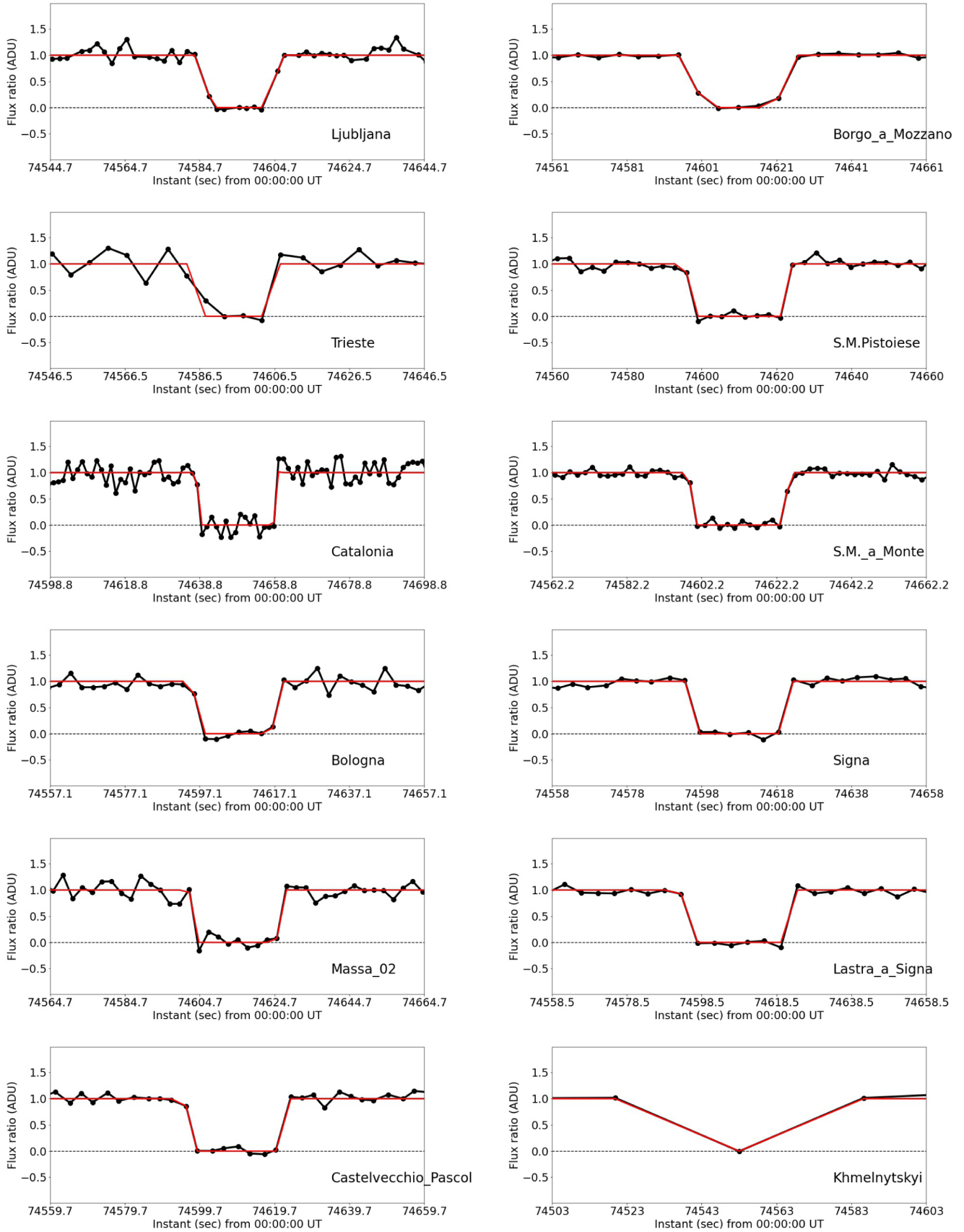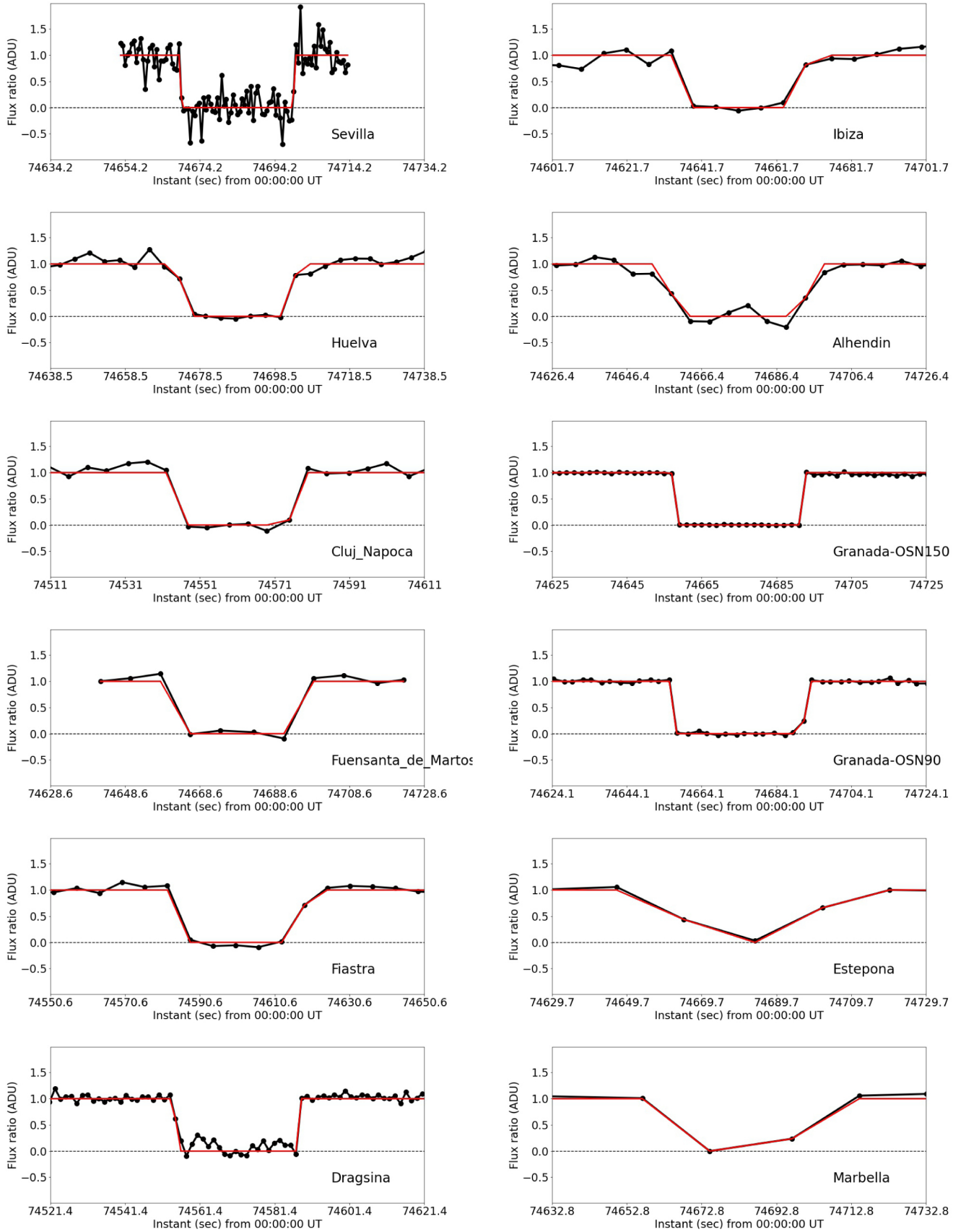
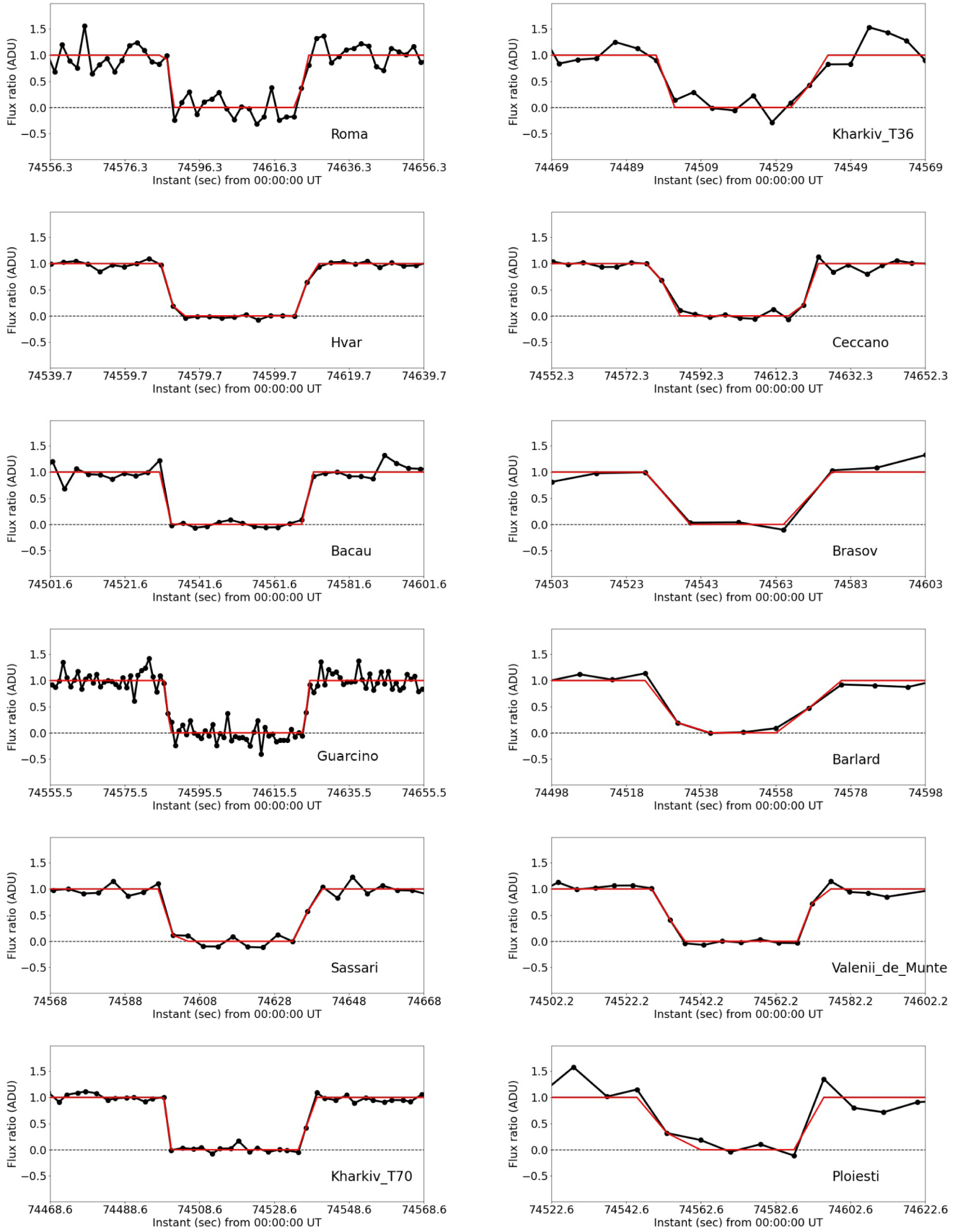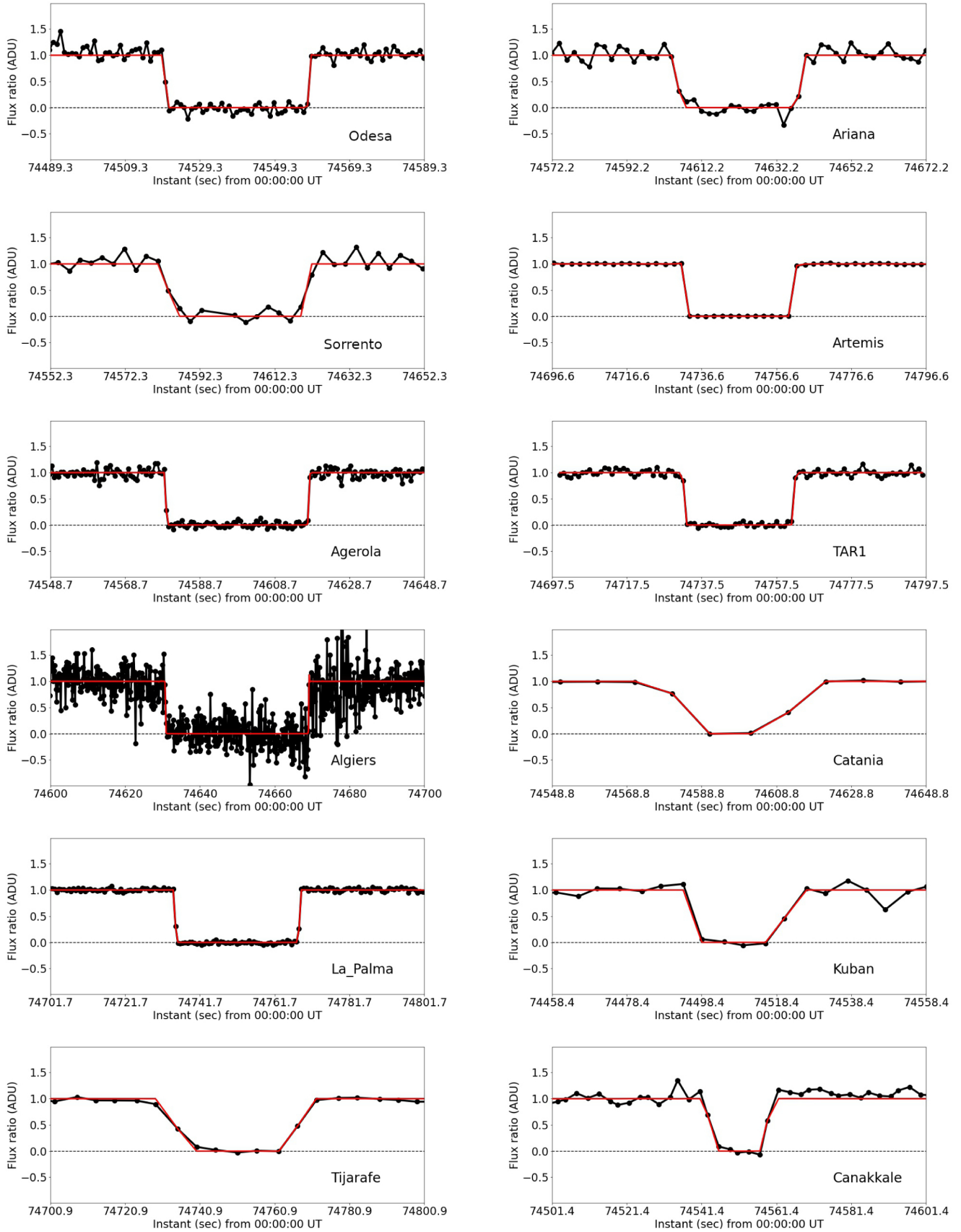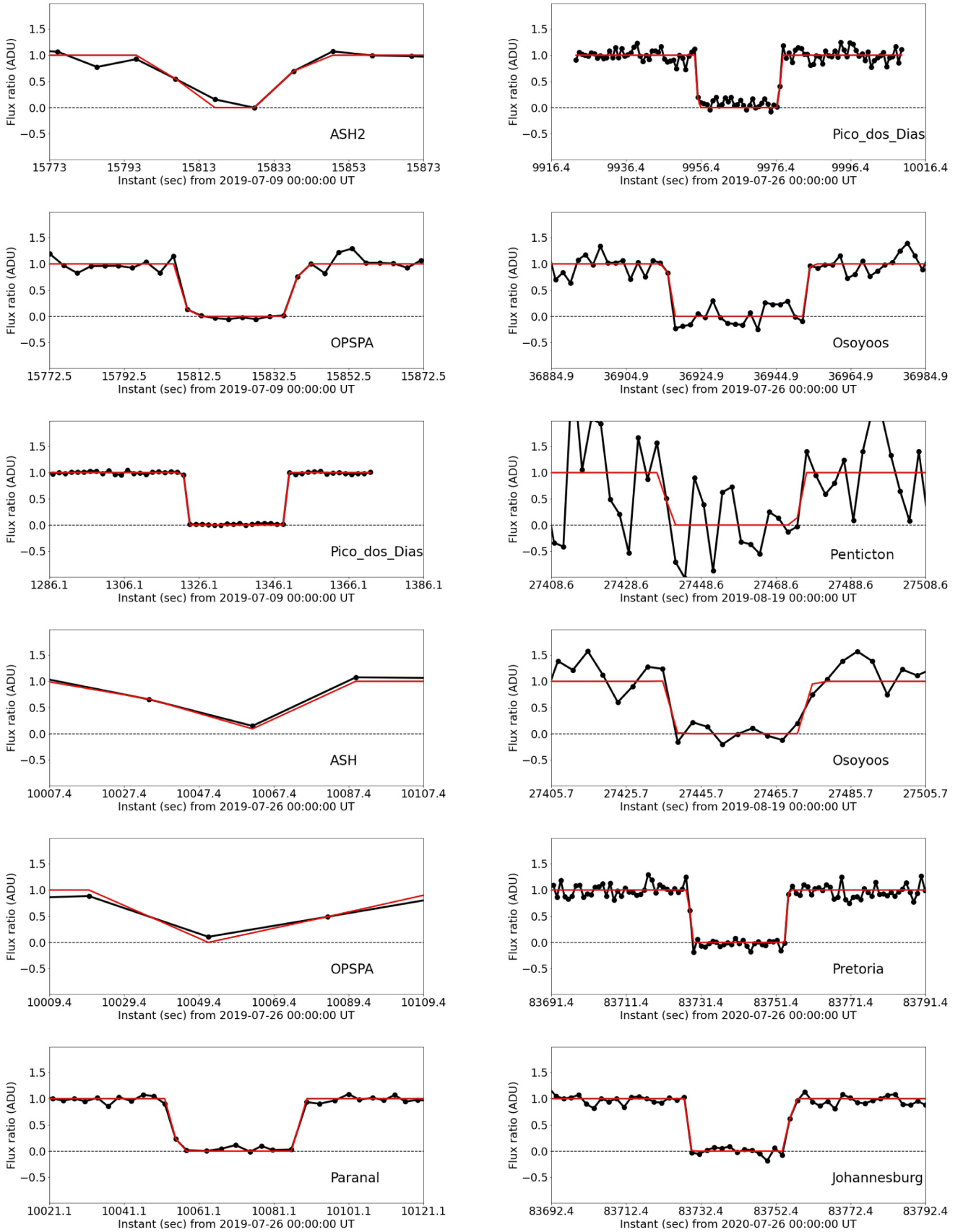Fig. C.1: continued.

Fig. C.1: continued.

Fig. C.1: continued.

Fig. C.1: continued.

Fig. C.2: Observed (black points) and calculated (red line) light curves for each site that observed a stellar occultation by 2002 MS$_4$, except the 8 August 2020 multichord event. See Table B.4 for observational details.
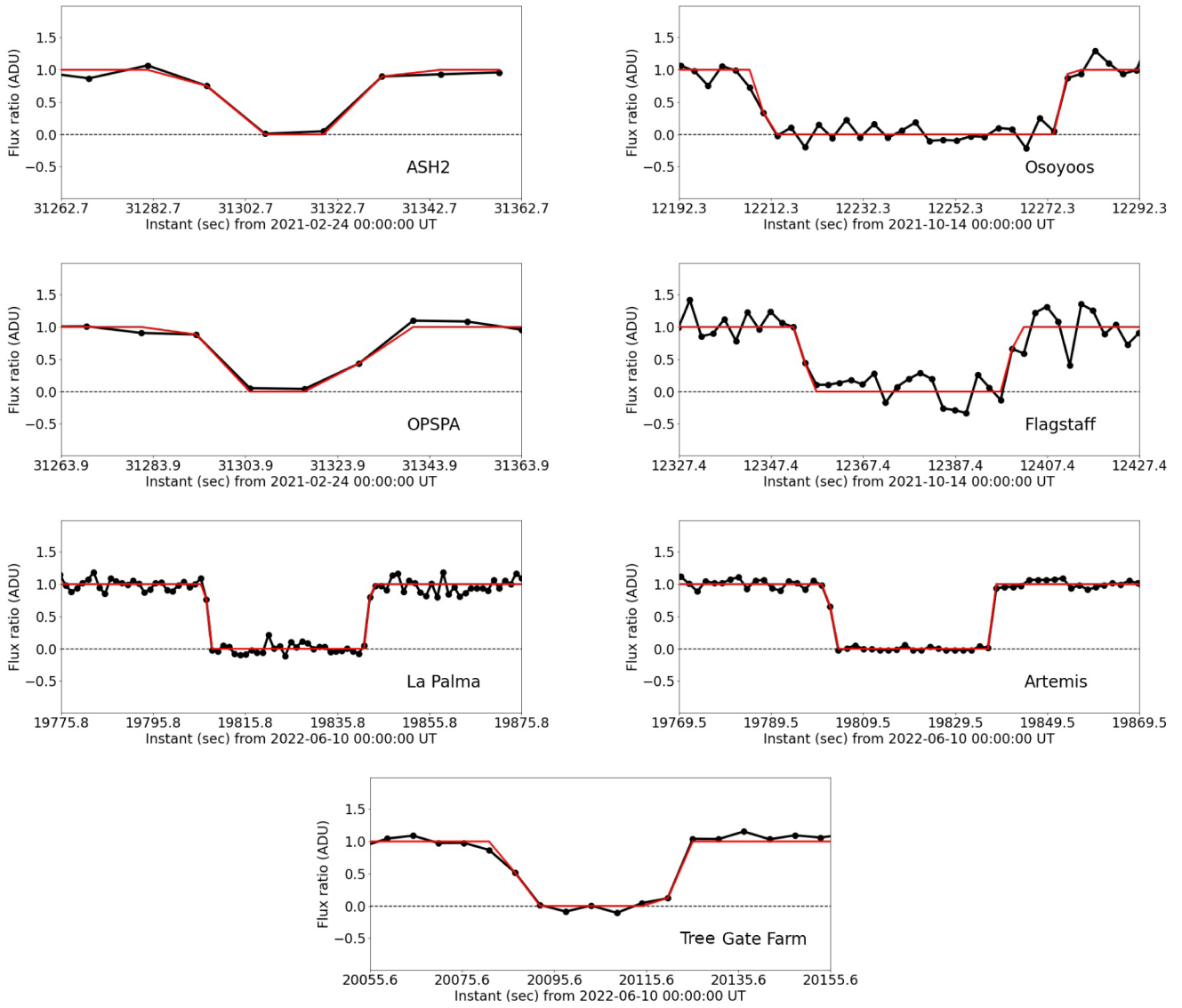
Fig. C.2: continued.

Appendix D: The unknown satellite hypothesis

Here, we present a short discussion about a hypothesis raised by the referee of a mutual event by an unknown satellite causing the 'bulge' on the observed limb of 2002 MS4 during the 8 August 2020 occultation. To explore such a possibility, I used all points between 5º and 25º to fit a circular limb of the putative satellite and the points between 50º and 340º to fit the main body limb. The satellite solutions were filtered by the negative part of the Varages light curve (orange line in Fig. D.1). As a result, we derived a diameter of ≈ 788 km for the main body and ≈ 213 for the putative satellite. Considering both projected areas at the sky plane, the area's equivalent diameter would be about 808 km. This result does not explain the diameter obtained from thermal measurements. Unless the putative satellite has a significant oblateness or if it irradiates more in the thermal than the 2002 MS$_4$ surface.
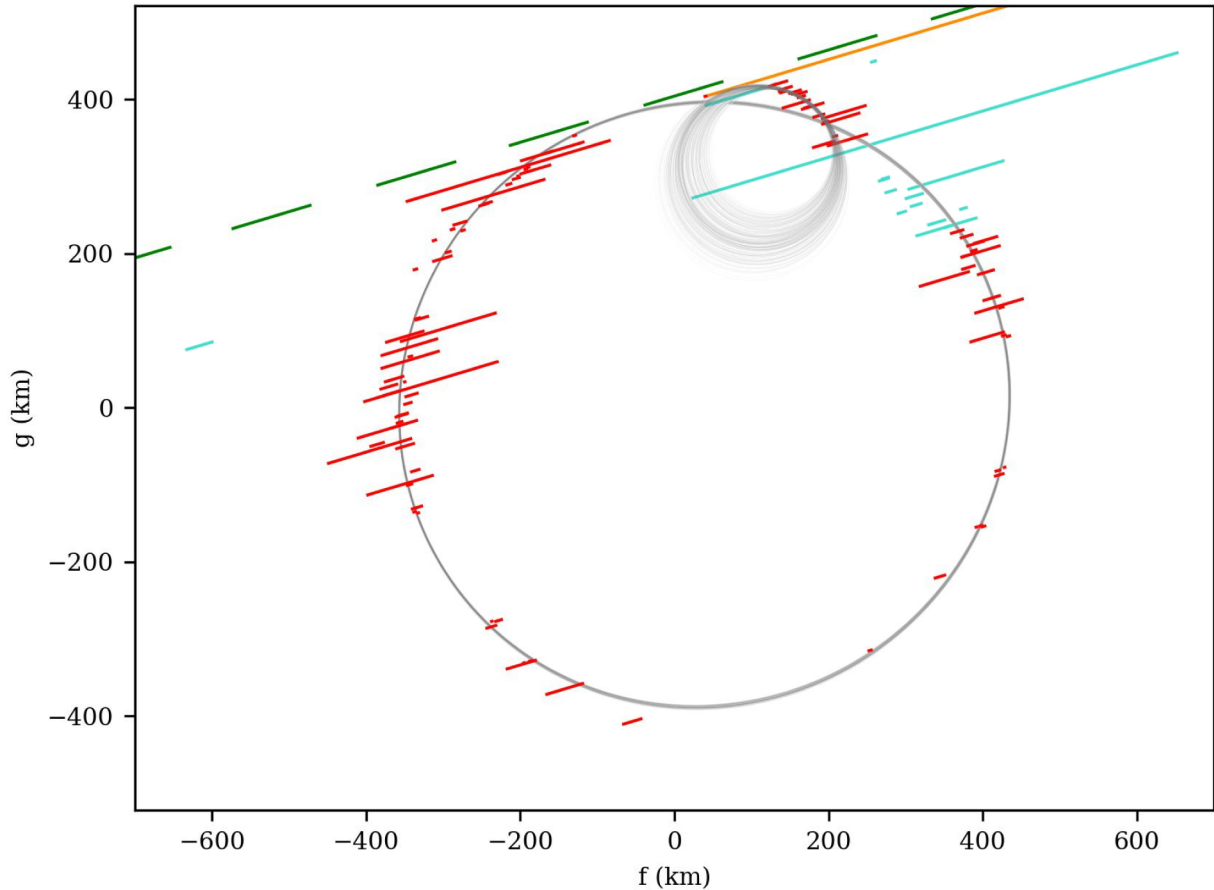

Fig. D.1: The gray regions show the 1σ fitted limb for the main body and the putative satellite. Green segments show each exposure acquired from Montsec station. This data set was the closest negative chord at North. The orange segment shows the negative part of the Varages light curve. Red segments are the observed immersion and emersion (1σ) instants used for the limb fitting. The turquoise segments are the immersion and emersion (1σ) instants not used in the fits.